LETTER

doi:10.1038/nature21424

Continuous-wave lasing in colloidal quantum dot solids enabled by facet-selective epitaxy

Fengjia Fan[1]*, Oleksandr Voznyy[1]*, Randy P. Sabatini[1]*, Kristopher T. Bicanic[1]*, Michael M. Adachi[1]†, James R. McBride[2], Kemar R. Reid[2], Young-Shin Park[3,4], Xiyan Li[1], Ankit Jain[1], Rafael Quintero-Bermudez[1], Mayuran Saravanapavanantham[1], Min Liu[1], Marek Korkusinski[5], Pawel Hawrylak[6], Victor I. Klimov[3], Sandra J. Rosenthal[2], Sjoerd Hoogland[1] & Edward H. Sargent[1]

Colloidal quantum dots (CQDs) feature a low degeneracy of electronic states at the band edges compared with the corresponding bulk material[1], as well as a narrow emission linewidth[2,3]. Unfortunately for potential laser applications, this degeneracy is incompletely lifted in the valence band, spreading the hole population among several states at room temperature[4–6]. This leads to increased optical gain thresholds, demanding high photoexcitation levels to achieve population inversion (more electrons in excited states than in ground states—the condition for optical gain). This, in turn, increases Auger recombination losses[7], limiting the gain lifetime to sub-nanoseconds and preventing steady laser action[8,9]. State degeneracy also broadens the photoluminescence linewidth at the single-particle level[10]. Here we demonstrate a way to decrease the band-edge degeneracy and single-dot photoluminescence linewidth in CQDs by means of uniform biaxial strain. We have developed a synthetic strategy that we term facet-selective epitaxy: we first switch off, and then switch on, shell growth on the (0001) facet of wurtzite CdSe cores, producing asymmetric compressive shells that create built-in biaxial strain, while still maintaining excellent surface passivation (preventing defect formation, which otherwise would cause non-radiative recombination losses). Our synthesis spreads the excitonic fine structure uniformly and sufficiently broadly that it prevents valence-band-edge states from being thermally depopulated. We thereby reduce the optical gain threshold and demonstrate continuous-wave lasing from CQD solids, expanding the library of solution-processed materials[11,12] that may be capable of continuous-wave lasing. The individual CQDs exhibit an ultra-narrow single-dot linewidth, and we successfully propagate this into the ensemble of CQDs.

At the band edge of CdSe CQDs, the electron level $1S_e$ is singly degenerate, with two spin projections; however, holes comprise two closely spaced $1S_{3/2}$ and $1P_{3/2}$ twofold-degenerate manifolds (Fig. 1), resulting in eight states when spin projections are taken into account[5,6]. In a hexagonal lattice, the crystal field lifts the degeneracy of the valence band. The use of oblate shapes can further increase the splitting, while the prolate shape counters the effect of the crystal field[4]. In spherical CQDs, the splitting is comparable to the thermal energy at room temperature, and therefore holes distribute among all eight states. This thermal population of many levels decreases the state filling of the valence band edge and increases the photoluminescence linewidth even in the absence of inhomogeneous broadening[4].

The optical gain condition in semiconductors can be fulfilled once the splitting between the quasi-Fermi levels of electrons (E_{Fe}) and holes (E_{Fh}) is larger than the bandgap (E_g) (Fig. 1)[13]. For a single electron and hole level with only spin degeneracy, populating the dot with one exciton translates the quasi-Fermi levels to the respective band edges, bringing the CQD to the onset of optical gain. By contrast, in the valence band of CdSe CQDs, a single charge carrier is spread among eight (including spin) valence states, greatly reducing the population per state (Fig. 1). The hole quasi-Fermi level thus remains further away from the band edge and the quasi-Fermi level splitting remains smaller than the bandgap. Extra excitons are therefore needed to achieve the required population of the band-edge states. For typical CdSe CQDs at room temperature, the threshold is achieved at $\langle N \rangle = 2.4 \pm 0.1$, where $\langle N \rangle$ is the average per-dot excitonic occupancy (see Methods subsection 'Simulation methods' and Extended Data Fig. 1d). Unfortunately, the increased exciton population counteracts the gain by speeding up Auger recombination[7], which substantially shortens the optical gain lifetime. Much attention has therefore been devoted to decreasing thresholds by using type-II heterostructures for reducing biexcitonic reabsorption[14]. Here we explore an alternative approach that is instead based on decreasing the level degeneracy.

The strategy of controlling level degeneracy using strain has proved successful in epitaxial quantum wells[15]. Hydrostatic compressive strain modifies the bandgap but does not affect the band-edge fine structure[16]. Biaxial strain, in contrast, lifts the degeneracy by having opposite effects on heavy and light holes. In CQDs, an external asymmetric compressive strain has been shown to split the hole states; however, this leads only to a broadening of the ensemble photoluminescence peak as a result of the random orientation of the CQDs[16]. Splitting of the band-edge exciton transition has also been observed in CQDs with a built-in asymmetric strain, yet narrower ensemble photoluminescence was not realized owing to the lack of strain uniformity[17,18].

If this splitting could be applied homogeneously to the CQDs in an ensemble, and made larger than the thermal energy, then the population of hole states would accumulate closer to the band edge, resulting in narrower emission linewidths (Fig. 1). At the same time, the effective degeneracy of the band-edge states would decrease, leading to lower optical gain thresholds closer to $\langle N \rangle = 1.9 \pm 0.1$ (see Methods subsection 'Simulation methods' and Extended Data Fig. 1e).

We sought therefore to create a synthesis route to introduce a built-in biaxial strain, homogeneous throughout the ensemble, while maintaining good surface passivation. In CdSe–CdS core–shell CQDs, the lattice mismatch between CdS and CdSe is around 3.9% (International Centre for Diffraction Data (ICDD) power diffraction files 65-3414 and 65-3415), leading to a hydrostatic compressive strain of the cores inside the spherical shells. We posited that sufficient biaxial strain could be achieved by growing an asymmetric shell. To demonstrate this, we started from the inherently asymmetric wurtzite crystal structure: its

[1]Department of Electrical and Computer Engineering, University of Toronto, 10 King's College Road, Toronto, Ontario M5S 3G4, Canada. [2]The Vanderbilt Institute of Nanoscale Science and Engineering, Vanderbilt University, Nashville, Tennessee 37235, USA. [3]Chemistry Division, Los Alamos National Laboratory, Los Alamos, New Mexico 87545, USA. [4]Center for High Technology Materials, University of New Mexico, Albuquerque, New Mexico 87131, USA. [5]Security and Disruptive Technologies, Emerging Technologies Division, National Research Council, Ottawa, Ontario K1A 0R6, Canada. [6]Physics Department, University of Ottawa, Ottawa, Ontario K1A 0R6, Canada. †Present address: School of Engineering Science, Simon Fraser University, 8888 University Dr Burnaby, British Columbia V5A 1S6, Canada.
*These authors contributed equally to this work.

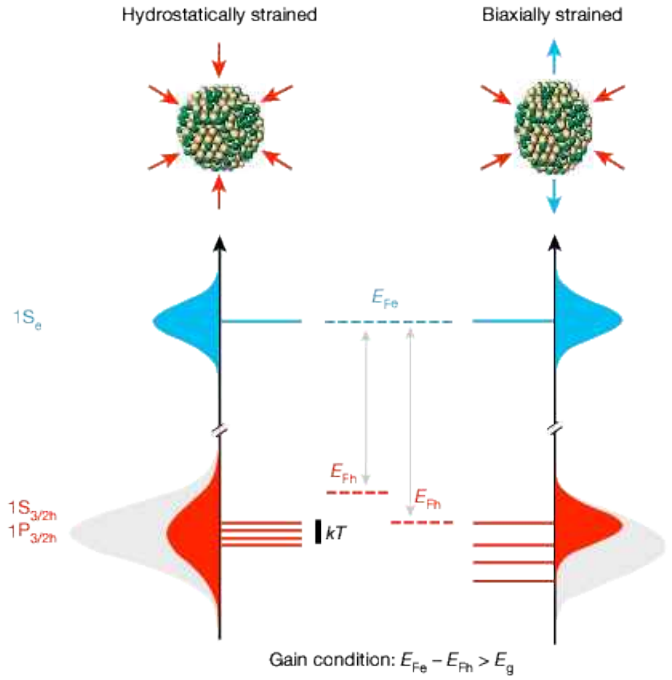

Figure 1 | CdSe CQD band-edge states, state filling and quasi-Fermi-level splitting under hydrostatic and biaxial strain. Red and blue arrows reveal the presence and absence of compressive strain, respectively. Green and gold balls represent Cd and Se atoms, respectively. On the left, the crystal field and shape anisotropy can lift the hole degeneracy, but the splitting remains comparable to the thermal energy, resulting in broadened photoluminescence and low state filling. This splitting is not affected by hydrostatic strain. On the right, biaxial strain causes additional splitting, concentrating the holes into the lowest-energy levels. Narrower photoluminescence and improved quasi-Fermi level splitting can be realized, lowering the gain threshold. E_{Fe} and E_{Fh} indicate the quasi-Fermi levels of electrons and holes, respectively, and kT denotes the thermal energy.

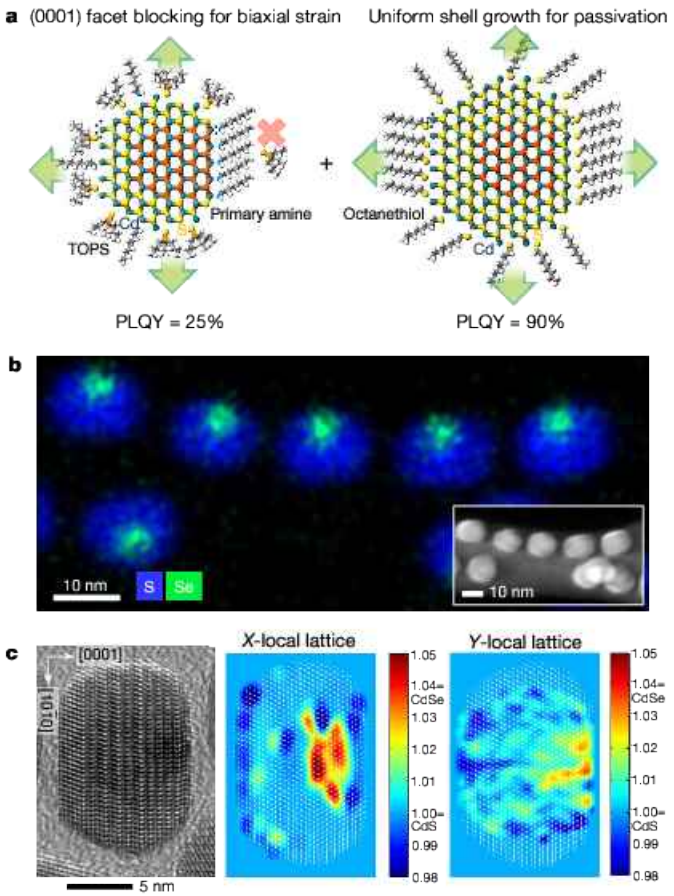

Figure 2 | Growth of asymmetric CQDs using facet-selective epitaxy. **a**, Facet-selective epitaxy growth mechanism. Green, red and yellow balls represent Cd, Se and S atoms, respectively. TOPS binds weakly to the (000$\bar{1}$) and {10$\bar{1}$0} facets but does not bind to the (0001) facet (dots indicate Cd dangling bonds). The primary amine can block the CdS shell growth (pink cross) on the CdSe (0001) facet while keeping the other facets growing (green arrows). Both facets can grow simultaneously when strongly binding octanethiol is used as a sulfur source. **b**, STEM-EDS mapping confirms the asymmetric shell on the core; the inset shows a HAADF-STEM image of asymmetric dots. **c**, An HRTEM image (left panel) and the corresponding local lattice constant mapping (middle and right panels) indicate biaxial strain.

{0001} facets are different from one another, the (0001) facet exposing Cd atoms with one dangling bond, and the (000$\bar{1}$) facet exposing Cd atoms with three dangling bonds. By tuning the relative reactivity of these two facets, rod-like CdSe–CdS core–shell nanostructures with centred[19] or off-centred cores[20] could be produced. However, this prolate shape counters the built-in crystal field effect, and therefore enhances—instead of lifting—the degeneracy[4].

Instead, we sought to take a different approach that would overcome the tendency of the polar lattice to take the undesired prolate crystal shape. Shell growth using trioctylphosphine sulfide (TOPS) has been shown to provide facet selectivity[21], and routes that employ thiols as precursors in combination with primary amine ligands produce isotropic shell growth[2]. We sought to amplify and then utilize these two desired effects in combination.

Density functional theory calculations revealed that octanethiol binds similarly on both {0001} CdSe facets, and much more strongly than the complementary ligand oleylamine (about 3 eV versus about 0.6 eV) (see Methods subsection 'Simulation methods' and Extended Data Table 1). Therefore, CdS tends to grow epitaxially on the CdSe surface without facet selectivity. By contrast, TOPS binds more weakly and very differently on (0001) and (000$\bar{1}$) facets (0 eV versus 0.5 eV), resulting in a high degree of facet selectivity. Since TOPS does not bind to the CdSe (0001) facet at all, we expect that even a weak ligand such as oleylamine could block CdS growth on this (0001) facet while allowing the (000$\bar{1}$) facet to grow slowly. The {10$\bar{1}$0} facets also grow epitaxially because they have a local surface structure similar to that of (000$\bar{1}$).

We therefore developed the facet-selective epitaxy protocol with the goal of growing an asymmetric shell in an oblate shape (see Methods subsection 'Synthesis methods' and Extended Data Fig. 2a). Since efficient (0001) blocking also leaves this facet unpassivated, it results in a low photoluminescence quantum yield (PLQY) of 25%, and the absence of the shell on one side leads to a short Auger lifetime (around 400 ps) (Extended Data Fig. 2c). We therefore grew a uniform second shell by switching the sulfur precursor to octanethiol after TOPS injection (see Methods subsection 'Synthesis methods', Fig. 2a, and Extended Data Fig. 2b). The final PLQY of the purified two-shell CQDs reaches 90% in solution and a PLQY of 75% in solid films (Extended Data Fig. 2c). The Auger recombination lifetime was extended to about 600 ps (Extended Data Fig. 2c).

The morphology of the asymmetric CQDs is shown in high-angle annular dark-field scanning transmission electron microscopy (HAADF-STEM) (inset in Fig. 2b) and bright-field transmission electron microscopy (Extended Data Fig. 2b) images. It shows an oblate shape with a diameter of 14.4 ± 0.7 nm and a height of 10.1 ± 0.6 nm, with a narrow ensemble size distribution. CdSe cores are consistently decentred inside the oblate CdS shell, as shown in STEM energy-dispersive X-ray spectroscopy (EDS) elemental mapping (Fig. 2b), a finding that reconfirms the facet-selective epitaxy growth mechanism.

High-resolution transmission electron microscopy (HRTEM) reveals lattice fringes along the [12$\bar{3}$0] zone axis, allowing for lattice constant mapping (Fig. 2c) to confirm that the lattice does exhibit the

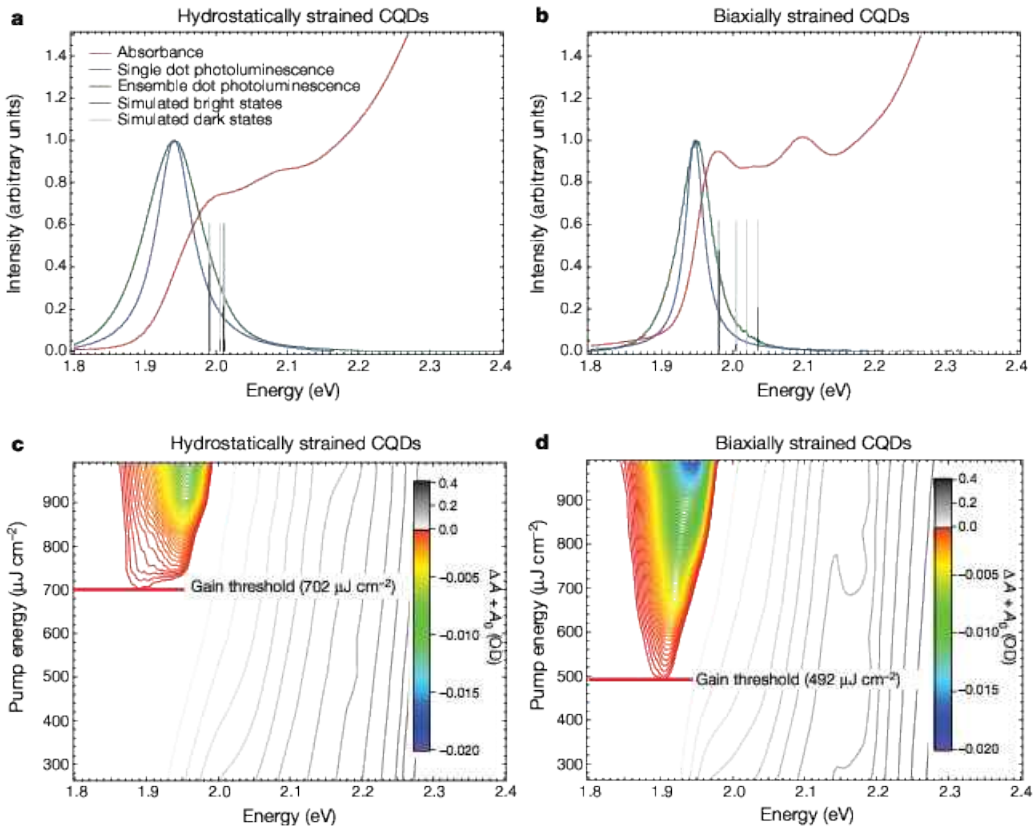

Figure 3 | Optical characterizations of CdSe–CdS core–shell CQDs. **a**, **b**, Ensemble absorbance and photoluminescence spectra, Lorentzian fits of single-dot photoluminescence spectra, and tight-binding model simulated exciton fine structure of hydrostatically strained (**a**) and biaxially strained (**b**) CQDs, respectively. **c**, **d**, Optical gain threshold measurements on the two different types of CQDs. The photexcitation energy was selected to be 2.18 eV to achieve comparable exciton populations with given photoexcitation fluence. The instantaneous total absorbance was collected 27 ps after pulsed excitation. ΔA, A_0 and OD denote absorbance change after excitation, ground-state absorbance, and optical density, respectively.

hypothesized biaxial strain (Extended Data Fig. 3a). On one side of the nanocrystal, distortion of the vertical lattice fringes suggests that the core is squeezed out by the compressive strain in the other two directions. The local lattice fringe spacing map along the horizontal direction (x axis) shows stronger deviation from the underlying CdS, approaching undistorted CdSe, implying that the strain along this horizontal direction has been released. The lattice fringe spacing along the vertical direction remains closer to CdS, indicating stronger compression of the core, and thus biaxial strain.

The absorbance spectra of hydrostatically and biaxially strained CQDs (Fig. 3a, b and Extended Data Fig. 4a) having similar average size (insets in Supplementary Fig. 1c, d) exhibit two striking differences: the first absorbance peak in biaxially strained CQDs is split into two, and it shows a much steeper absorbance edge. A series of samples with different thicknesses of the first asymmetric shell reveal a progressive splitting of the first exciton peak (Extended Data Fig. 5a–g), reaching a maximum of 67 meV. After a second uniform shell is added, the splitting decreases slightly to 55 meV (Fig. 3b).

These interpretations were supported by tight-binding atomistic simulations (see Methods subsection 'Simulation methods', Supplementary Table 1, Extended Data Fig. 3, and Supplementary Fig. 2). In hydrostatically strained CQDs, the bright transitions within the first exciton manifold are split by the crystal field by only 20 meV (Fig. 3a and Extended Data Fig. 3c, d), while in the presence of biaxial strain, the splitting increases to about 55 meV (Fig. 3b and Extended Data Fig. 3c, d). This partially explains the impressively sharp absorbance edge in the biaxially strained case. For the same reason, the Stokes shift of the biaxially strained CQDs is a mere 24 meV, much smaller than that of CQDs under hydrostatic strain (40 meV).

Single-dot and ensemble photoluminescence measurements were carried out to probe the emission states and the broadenings for the two dot types. A short binning time of 50 ms was applied to minimize spectral diffusion. As in prior reports for similarly sized CQDs[22], hydrostatically strained CQDs show full-width at half-maximum (FWHM) values for single-dot and ensemble photoluminescence of 63 ± 7 meV and 95 meV (Fig. 3a and Extended Data Fig. 6a, c), respectively, typical for giant-shell CQDs[22]. In striking contrast, the biaxially strained core–shell CQDs have a single-dot photoluminescence FWHM as narrow as 36 ± 3 meV, compared to the 54 meV in ensemble (Fig. 3b and Extended Data Fig. 6b, d). The reduced broadening also contributes to the sharp absorbance edge and better resolved peaks in the absorbance spectra of biaxially strained CQDs. This single-dot emission linewidth is even narrower than that from single nanoplatelets[23,24], whose light and heavy holes are well separated by extreme quantum confinement. This twofold reduction of the single-dot linewidth in biaxially strained dots can be explained as follows: (1) the exciton fine structure has been substantially spread out (to an extent that notably exceeds the thermal energy); and (2) the exciton coupling to longitudinal optical phonons has been suppressed in this asymmetric core–shell structure[10]. An approximately 20% narrowing in ensemble photoluminescence linewidth is achieved here compared to previous narrowest-linewidth CQDs[2] and core–shell nanoplatelets[25,26]. An even narrower ensemble photoluminescence (FWHM of 50 meV) can be obtained in biaxially strained CQDs having thinner CdS shells (Extended Data Fig. 5d).

Ultrafast transient absorption spectroscopy was used to measure the optical gain threshold of both the biaxially and hydrostatically strained CQDs. In the femtosecond and picosecond regimes, the optical gain threshold of CQDs is affected by two key parameters: (1) the absorption

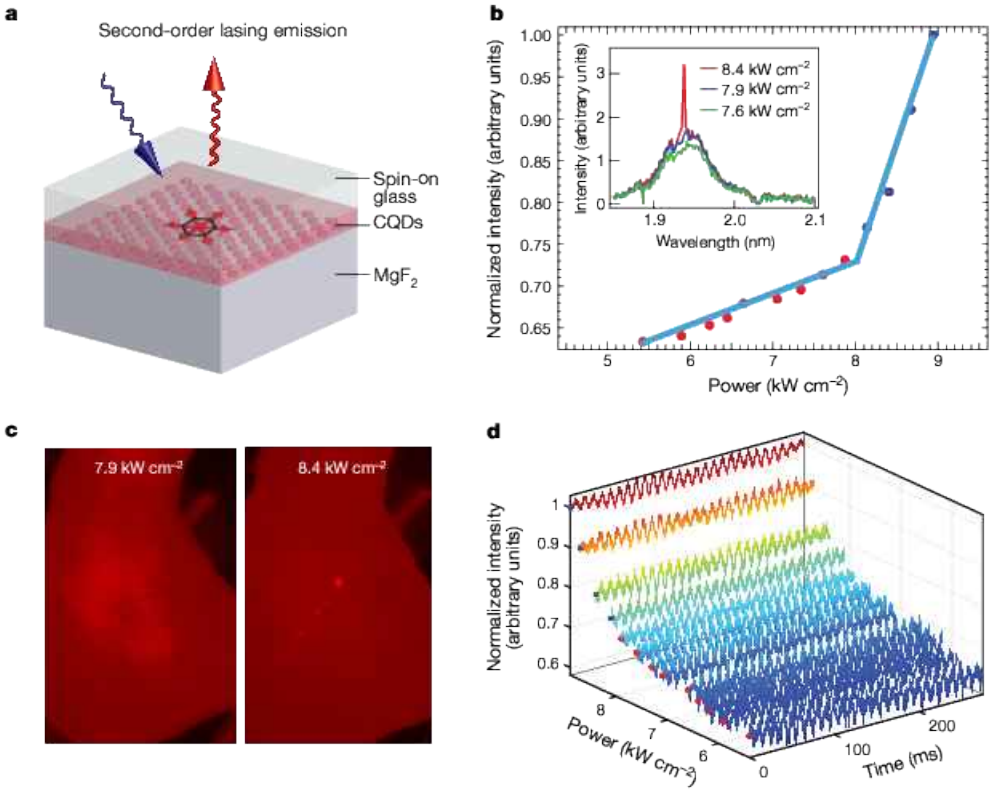

Figure 4 | Continuous-wave PC-DFB CQD laser. a, Schematic of the PC-DFB device used for lasing. **b**, Normalized integration of emitted signal (shown in Fig. 4d) as a function of peak power. Insets show emission spectra above and below the lasing threshold. **c**, Photographs showing emission below and above the threshold, respectively. Above the threshold, bright lasing spots are visible. Images were converted to intensities and displayed with a red colour scale. **d**, Time traces of normalized emission intensity of the PC-DFB laser as a function of time and incident power while excited with continuous-wave laser.

cross-section, which controls how many excitons are generated at a given photoexcitation power density; and (2) the average excitons-per-dot occupancy $\langle N \rangle$ needed to reach the point where stimulated emission overcomes absorption. To decouple the effect of the absorption cross-section, we used identical cores to grow hydrostatically strained and biaxially strained CQDs, and then performed transient absorption measurements by photoexciting mainly the cores (2.18 eV, 250-fs pulses). Gain thresholds of 490 μJ cm^{-2} and 700 μJ cm^{-2} for biaxially and hydrostatically strained dots in solution, respectively, indicate a factor of 1.43 reduction in per-pulse fluence for the former structures (Fig. 3c, d and Supplementary Fig. 3c, d). The corresponding exciton occupancies were calculated by multiplying the photoexcitation fluences and the measured absorption cross-sections (see Methods subsection 'Characterization methods' and Extended Data Fig. 4d), and values of $\langle N \rangle = 2.3 \pm 0.4$ and 3.2 ± 0.6 were obtained for the biaxially and hydrostatically strained dots, respectively. This trend is consistent with the $\langle N \rangle = 1.9 \pm 0.1$ and 2.4 ± 0.1 values obtained from numerical gain modelling (see Methods subsection 'Simulation methods' and Extended Data Fig. 1). Simulations show that the differences in linewidth contribute only about 2% to threshold improvement (Extended Data Fig. 1d).

In lasers, CQDs are usually photoexcited above the shell bandgap in order to take advantage of the large absorption cross-section of the shell and thus achieve the threshold occupancy $\langle N \rangle$ at lower external photoexcitation power[27]. We therefore acquired amplified spontaneous emission (ASE) thresholds using shell photoexcitation. Biaxially and hydrostatically strained dots show ASE thresholds of 26 μJ cm^{-2} and 36 μJ cm^{-2} per pulse, respectively (Extended Data Fig. 7a–d and Supplementary Fig. 2). Lower ASE thresholds of 14 μJ cm^{-2} and 22 μJ cm^{-2} were observed when laser pulses of 250 fs (3.49 eV) were used instead (Extended Data Fig. 7e, f); this can be attributed to the reduction of Auger recombination losses at the pumping stage. The 1.4- to 1.6-fold reduction in the ASE threshold for the biaxially strained sample is attributed to the reduced gain threshold, since the biexciton Auger lifetime (Extended Data Fig. 8) and absorption cross-section (Extended Data Fig. 4d) remain similar for the two samples and thus do not contribute to the observed improvement.

To demonstrate sustained lasing, we incorporated a film of biaxially strained CQDs into a photonic crystal distributed feedback (PC-DFB) optical cavity (see Methods subsection 'Characterization methods', Fig. 4a, and Supplementary Fig. 5). The PC-DFB cavity was photoexcited at 2.81 eV using a continuous-wave laser. The excitation-power-dependent emission intensities show lasing thresholds of around 6.4–8.4 kW cm^{-2} (Fig. 4b and Extended Data Fig. 9a–g), which are about seven times lower than that of the previously reported CQD laser (50 kW cm^{-2}) using a similar cavity[28]. As a result of the sublinearity of photoluminescence (owing to Auger recombination), the y intercept appears larger than zero. The lasing emission peak wavelength is 1.94 eV (inset to Fig. 4b), with a FWHM of about 3 meV (limited by the resolution of our spectrometer). The directionality of the laser beam was displayed by placing a card about 5 cm away from the sample. Below the threshold, diffuse emission due to photoluminescence is visible, whereas above the threshold, several bright laser spots are visible, showing almost no divergence, in the centre of the emission beam (Fig. 4c). The lasing output was monitored using an oscilloscope, and we found that the devices did indeed lase continuously. The traces exhibit threshold behaviour as well as steady signals at each excitation power (Fig. 4d). The fluctuation of the signal originates from electronic noise induced by the acousto-optic modulator on the oscilloscope (Extended Data Fig. 9f, g). Continuous-wave lasing lasted for approximately 30 min and 10 min before thresholds increased, in devices with thresholds of 6.4 kW cm^{-2} and 8.4 kW cm^{-2}, respectively. The hydrostatically strained CQDs in the same PC-DFB cavity exhibit a lasing

threshold (20–24 kW cm^{-2}, Extended Data Fig. 9h, i) insufficiently low for continuous-wave operation[28], achieving at most 30 μs of sustained lasing.

Online Content Methods, along with any additional Extended Data display items and Source Data, are available in the online version of the paper; references unique to these sections appear only in the online paper.

Received 2 July 2016; accepted 23 January 2017.
Published online 20 March 2017.

1. Klimov, V. I. *et al.* Optical gain and stimulated emission in nanocrystal quantum dots. *Science* **290,** 314–317 (2000).
2. Chen, O. *et al.* Compact high-quality CdSe-CdS core-shell nanocrystals with narrow emission linewidths and suppressed blinking. *Nat. Mater.* **12,** 445–451 (2013).
3. Dai, X. *et al.* Solution-processed, high-performance light-emitting diodes based on quantum dots. *Nature* **515,** 96–99 (2014).
4. Efros, A. L. *et al.* Band-edge exciton in quantum dots of semiconductors with a degenerate valence band: dark and bright exciton states. *Phys. Rev. B* **54,** 4843–4856 (1996).
5. Korkusinski, M., Voznyy, O. & Hawrylak, P. Fine structure and size dependence of exciton and biexciton optical spectra in CdSe nanocrystals. *Phys. Rev. B* **82,** 245304 (2010).
6. Franceschetti, A., Fu, H., Wang, L. W. & Zunger, A. Many-body pseudopotential theory of excitons in InP and CdSe quantum dots. *Phys. Rev. B* **60,** 1819–1829 (1999).
7. Klimov, V. I. Multicarrier interactions in semiconductor nanocrystals in relation to the phenomena of auger recombination and carrier multiplication. *Annu. Rev. Condens. Matter Phys.* **5,** 285–316 (2014).
8. Guilhabert, B. *et al.* Nanosecond colloidal quantum dot lasers for sensing. *Opt. Express* **22,** 7308–7319 (2014).
9. McLellan, L. J., Guilhabert, B., Laurand, N. & Dawson, M. D. $CdS_{(x)}Se_{(1-x)}$/ZnS semiconductor nanocrystal laser with sub 10kW/cm^2 threshold and 40nJ emission output at 600 nm. *Opt. Express* **24,** A146–A153 (2016).
10. Cui, J. *et al.* Evolution of the single-nanocrystal photoluminescence linewidth with size and shell: implications for exciton-phonon coupling and the optimization of spectral linewidths. *Nano Lett.* **16,** 289–296 (2016).
11. Grim, J. Q. *et al.* Continuous-wave biexciton lasing at room temperature using solution-processed quantum wells. *Nat. Nanotechnol.* **9,** 891–895 (2014).
12. Iyer, V. H., Mahadevu, R. & Pandey, A. Low threshold quantum dot lasers. *J. Phys. Chem. Lett.* **7,** 1244–1248 (2016).
13. Bernard, M. G. A. & Duraffourg, G. Laser conditions in semiconductors. *Phys. Status Solidi B* **1,** 699–703 (1961).
14. Klimov, V. I. *et al.* Single-exciton optical gain in semiconductor nanocrystals. *Nature* **447,** 441–446 (2007).
15. Yablonovitch, E. & Kane, E. O. Reduction of lasing threshold current-density by the lowering of valence band effective mass. *J. Lightwave Technol.* **4,** 504–506 (1986).
16. Choi, C. L., Koski, K. J., Sivasankar, S. & Alivisatos, A. P. Strain-dependent photoluminescence behavior of CdSe/CdS nanocrystals with spherical, linear, and branched topologies. *Nano Lett.* **9,** 3544–3549 (2009).
17. Veilleux, V. *et al.* Strain-induced effects in colloidal quantum dots; lifetime measurements and blinking statistics. *Nanotechnology* **21,** 134024 (2010).
18. Cassette, E. *et al.* Colloidal CdSe/CdS dot-in-plate nanocrystals with 2D-polarized emission. *ACS Nano* **6,** 6741–6750 (2012).
19. Christodoulou, S. *et al.* Band structure engineering via piezoelectric fields in strained anisotropic CdSe/CdS nanocrystals. *Nat. Commun.* **6,** 7905 (2015).
20. Talapin, D. V. *et al.* Highly emissive colloidal CdSe/CdS heterostructures of mixed dimensionality. *Nano Lett.* **3,** 1677–1681 (2003).
21. Christodoulou, S. *et al.* Synthesis of highly luminescent wurtzite CdSe/CdS giant-shell nanocrystals using a fast continuous injection route. *J. Mater. Chem. C* **2,** 3439–3447 (2014).
22. Cui, J. *et al.* Direct probe of spectral inhomogeneity reveals synthetic tunability of single-nanocrystal spectral linewidths. *Nat. Chem.* **5,** 602–606 (2013).
23. Tessier, M. D., Javaux, C., Maksimovic, I., Loriette, V. & Dubertret, B. Spectroscopy of single CdSe nanoplatelets. *ACS Nano* **6,** 6751–6758 (2012).
24. Tessier, M. D. *et al.* Spectroscopy of colloidal semiconductor core/shell nanoplatelets with high quantum yield. *Nano Lett.* **13,** 3321–3328 (2013).
25. Mahler, B., Nadal, B., Bouet, C., Patriarche, G. & Dubertret, B. Core/shell colloidal semiconductor nanoplatelets. *J. Am. Chem. Soc.* **134,** 18591–18598 (2012).
26. Ithurria, S. & Talapin, D. V. Colloidal atomic layer deposition (c-ALD) using self-limiting reactions at nanocrystal surface coupled to phase transfer between polar and nonpolar media. *J. Am. Chem. Soc.* **134,** 18585–18590 (2012).
27. Dang, C. *et al.* Red, green and blue lasing enabled by single-exciton gain in colloidal quantum dot films. *Nat. Nanotechnol.* **7,** 335–339 (2012).
28. Adachi, M. M. *et al.* Microsecond-sustained lasing from colloidal quantum dot solids. *Nat. Commun.* **6,** 8694 (2015).

Supplementary Information is available in the online version of the paper.

Acknowledgements This publication is based in part on work supported the Ontario Research Fund-Research Excellence Program and by the Natural Sciences and Engineering Research Council (NSERC) of Canada. Computations were performed on the GPC supercomputer at the SciNet HPC Consortium. SciNet is funded by: the Canada Foundation for Innovation under the auspices of Compute Canada; the Government of Ontario; the Ontario Research Fund–Research Excellence; and the University of Toronto. Y.-S.P. and V.I.K. are supported by the Chemical Sciences, Biosciences and Geosciences Division, Office of Basic Energy Sciences, Office of Science, US Department of Energy. J.R.M., K.R.R. and S.J.R. acknowledge funding from the National Science Foundation (CHE-1506587 and EPS 1004083). A.J. is supported by the IBM Canada Research and Development Center through the Southern Ontario Smart Computing Innovation Platform (SOSCIP) postdoctoral fellowship. The SOSCIP consortium is funded by the Ontario Government and the Federal Economic Development Agency for Southern Ontario. P.H. acknowledges support by the University of Ottawa Research Chair in Quantum Theory of Materials, Nanostructures and Devices. We thank C. Wang, H. Liang, N. Hossain, X. Zheng, Z. Shi, G. Walters, E. Palmiano, R. Wolowiec and D. Kopilovic for discussions during this work.

Author Contributions F.F. and O.V. conceived the idea. F.F. developed the CQD synthesis and performed transient absorption measurements. O.V. carried out theoretical simulations. R.P.S. and K.T.B. designed, fabricated, and characterized the continuous-wave PC-DFB laser devices and films. M.M.A. contributed to PC-DFB laser design, device and film characterizations. J.R.M., K.R.R. and S.J.R. collected STEM-EDS elemental mapping and single-dot photoluminescence linewidth data. Y.-S.P. and V.I.K. contributed to single-dot and low-temperature photoluminescence decay measurements, and modelling of band-edge state degeneracies in relation to gain thresholds. X.L. and M.S. assisted in CQD synthesis optimizations. A.J., M.K. and P.H. contributed to theoretical simulations. R.Q.-B. performed HRTEM lattice analysis. M.L. performed SEM imaging. F.F., O.V., R.P.S., K.T.B. and E.H.S. wrote the manuscript. S.H. and E.H.S. supervised the project. All authors discussed the results and assisted in the preparation of the manuscript.

Author Information Reprints and permissions information is available at www.nature.com/reprints. The authors declare no competing financial interests. Readers are welcome to comment on the online version of the paper. Correspondence and requests for materials should be addressed to E.H.S. (ted.sargent@utoronto.ca).

Reviewer Information *Nature* thanks T. Krauss and the other anonymous reviewer(s) for their contribution to the peer review of this work.

METHODS

Chemicals and synthesis. Cadmium oxide (>99.99%), sulfur powder (S, >99.5%), selenium powder (Se, >99.99%), oleylamine (>98% primary amine), octadecene (90%), oleic acid (90%), trioctylphosphine (90%), tri-butylphosphine (97%), trioctylphosphine oxide (99%), octadecylphosphonic acid (97%), 1-octanethiol (>98.5%), thionyl chloride ($SOCl_2$), toluene (anhydrous, 99.8%), hexane (anhydrous, 95%), acetone (99.5%) and acetonitrile (anhydrous, 99.8%) were purchased from Sigma-Aldrich and used without further purification.

CdSe CQDs were synthesized by scaling up an existing literature procedure by eight times[29]. CQDs exhibiting an exciton peak at 590 nm were synthesized as a result of about 3 min growth. 2.98 g cadmium oxide was fully dissolved in 40 ml oleic acid at 170 °C under vacuum and then nitrogen to obtain Cd-oleate. TOPS was prepared by mixing and magnetically stirring 960 mg sulfur powder in 16 ml trioctylphosphine inside the glovebox.

Facet-selective epitaxy. The first asymmetric shell was grown as follows. By measuring the absorbance at peak exciton (590 nm) with 1 mm light path length cuvette, we quantified CdSe CQDs[30]. A 5.8 ml CdSe CQD in hexane dispersion with an optical density of 1 at the exciton peak was added to a mixture of 42 ml octadecene and 6 ml oleylamine in a 500 ml flask, and pumped in vacuum at 100 °C to evaporate hexane; then the solution was heated to 300 °C and kept for 0.5 h. As-prepared 9 ml Cd-oleate was diluted in 15 ml octadecene and 3 ml TOPS in 21 ml octadecene as a sulfur precursor, respectively. Cd-oleate and TOPS solutions were injected simultaneously and continuously at a rate of 6 ml h^{-1}.

The second uniform shell was grown as follows: 4 ml Cd-oleate diluted in 20 ml octadecene and 427 μl 1-octanethiol diluted in 23.6 ml octadecene were continuously injected at a speed of 12 ml h^{-1} to grow the second shell. The reaction temperature was elevated to 310 °C before injection. After a 13 ml injection of Cd-oleate into octadecene solution, 5 ml oleylamine was injected into the solution to improve the dispersibility of the CQDs.

Core-shell CQD purification was performed as follows: when the injection was complete, the final reaction mixture was naturally cooled to around 50 °C and transferred into 50 ml plastic centrifuge tubes; no anti-solvent was added and the precipitation was collected after 3 min centrifugation at a speed of 6,000 r.p.m. 20 ml hexane was added into the centrifuge tubes to disperse the CQDs, and acetone was added dropwise until the CQDs started to aggregate. The precipitation was collected again by 3 min centrifugation at a speed of 6,000 r.p.m.; this dispersing and precipitation process was repeated three times to completely remove smaller CdS CQDs. This purification process is critical for obtaining low-ASE-threshold and high-PLQY CQDs, because the binding energy between TOPS and CdSe CQDs is weak (Extended Data Table 1) and only 30% of the CdS precursor is deposited onto CdSe cores. The final CQDs were re-dispersed in octane with the first exciton peak absorbance in 1 mm light path length fixed as 0.25.

The asymmetric CQD 3 sample was synthesized by growing only an asymmetric shell, as mentioned above; no secondary uniform shell was grown. The asymmetric CQD 2 sample was synthesized with a protocol similar to that of the asymmetric CQD 3 sample, except that the reaction solvent (42 ml octadecene and 6 ml oleylamine) was substituted with 24 ml octadecene and 24 ml oleylamine. The asymmetric CQD 1 sample was synthesized by repeating the asymmetric CQD 2 shell growth twice. The CQDs were washed using the above-mentioned purification process. See Extended Data Fig. 5 for absorbance and photoluminescence spectra.

To obtain hydrostatically strained CQDs, conventional symmetric CQDs were synthesized by modifying the methods of refs 2 and 31. A 8.8 ml CdSe core dispersion with an optical density of 1 at the exciton peak 590 nm was added to a mixture of 24 ml octadecene and 24 ml oleylamine in a 500 ml flask, and pumped in vacuum at 100 °C to evaporate hexane; then the solution was heated to 310 °C and kept for 0.5 h. 6 ml as-prepared Cd-oleate was diluted in 18 ml octadecene and 640 μl octanethiol in 23.36 ml octadecene as sulfur precursor. Cd-oleate and octanethiol solutions were injected simultaneously and continuously at a rate of 12 ml h^{-1}. After injection, 4 ml oleic acid was injected and the solution was further annealed at 310 °C for 10 min.

To achieve chloride ligand exchange, 500 μl of the above CQDs dispersion (first peak exciton OD = 0.25) was vacuum dried and then dispersed in 1 ml toluene solution, 1.25 ml tributylphosphine, followed by 1 ml $SOCl_2$ in toluene solution (volume ratio of 20 μl $SOCl_2$:1 ml toluene) was added into the CQDs in toluene dispersion inside the glovebox. The CQDs precipitated immediately and the resulting dispersion was transferred out of the glovebox and subsequently ultrasonicated for 1 min. After the exchange, anhydrous hexane was added to precipitate the CQDs completely before centrifugation at 6,000 r.p.m. CQDs were purified with three cycles of adding anhydrous acetone to disperse the CQDs and adding hexane to precipitate the CQDs dispersion. The chloride-ligand-terminated CQDs were finally dispersed in 750 μl anhydrous acetonitrile for the fabrication of the laser devices.

Characterization methods. CQDs in hexane dispersion were collected into a 1 mm path length quartz cuvette, and ensemble absorbance was measured on the PerkinElmer Lambda 950 UV/Vis/NIR spectrophotometer over the excitation range 400–800 nm. Ensemble photoluminescence spectra and single-exciton decay data of diluted solution samples were collected on the Horiba Flurolog TCSPC system with an iHR 320 monochromator and a PPO-900 detector. An integrating sphere was used for film and solution PLQY measurement.

To obtain single-CQD photoluminescence measurements, dilute solutions of CQDs in hexanes were drop-cast on quartz substrates. Single-particle photoluminescence measurements were conducted using a custom-built confocal microscope previously described[32]. Samples were excited by a 400 nm, 76 MHz pulsed laser at low excitation powers (about 5 W cm^{-2}). Photoluminescence emission from individual quantum dots was collected through the objective (Olympus, 1.2 numerical aperture), projected onto the entrance slit of an Ocean Optics QE spectrometer (600 lines mm^{-1}) equipped with a Hamamatsu, back-illuminated cooled charge-coupled device (CCD) array for detection. Time series of integrated spectra were acquired at room temperature with integration times of 50 ms.

To obtain transient absorption measurements, the 1,030 nm fundamental (5 kHz) was produced by a ytterbium-doped potassium gadolinium tungstate (Yb:KGW) regenerative amplifier (Pharos, Light Conversion). A portion of this beam was sent through an optical parametric amplifier (Orpheus, Light Conversion) to generate the 2.18 eV photoexcitation pulse (pulse duration about 250 fs). Both the photoexcitation and fundamental were sent into an optical bench (Helios, Ultrafast). The fundamental, after passing through a delay stage, was focused into a sapphire crystal, generating the probe as a white-light continuum. The frequency of the photoexcitation pulse was reduced to 2.5 kHz using a chopper. Both beams were then focused onto the sample, which was housed in a 1 mm cuvette. The probe was then detected by a CCD (Helios, Ultrafast). Samples were translated 1 mm s^{-1} during the measurements.

CQDs were dispersed in hexane to measure the absorption cross-section[33] $\sigma = 2.303A/cl$, where σ is the absorption cross-section of CQDs, A is the absorbance of CQD in hexane dispersion at a given wavelength, c is the number of nanocrystals per cubic centimetre, l is the light path length of the cuvette in centimetres, and c was calculated as follows:

$$c = \frac{N_{\text{total,Cd}}}{N_{\text{single,Cd}} \times V}$$

CQDs dispersion (V = 0.4 ml with known absorbance was digested in nitric acid and diluted to 10 ml aqueous solution. Inductively coupled plasma optical emission spectroscopy (ICP-OES) (using a Optima 7300 ICP AES) was applied to determine the total amount of Cd atoms ($N_{\text{total,Cd}}$), the single-dot Cd atom numbers ($N_{\text{single,Cd}}$) were estimated from the volume of a single CQD, which were determined from the TEM images (Extended Data Fig. 2b and Supplementary Fig. 1). Hydrostatically strained dots were assumed to have circular cone shapes with a bottom radius of 15 ± 1 nm and a height of 15.2 ± 1 nm. Biaxially strained dots were considered to be hexagonal prisms with an average lateral dimension of 12 ± 1 nm and height of 10 nm. Total volumes of 907 ± 180 nm^3 and 935 ± 157 nm^3 were obtained, respectively. See Extended Data Fig. 4c and d for the wavelength-resolved absorption cross-sections of two types of CQDs.

HRTEM and STEM-EDS samples were prepared by adding a drop of the solution of CQDs onto an ultrathin-carbon film on lacey-carbon support film (Ted Pella 01824) and were baked under high vacuum at 165 °C overnight and subsequently imaged using a Tecnai Osiris TEM/STEM operating at 200 kV. Drift-corrected STEM-EDS maps were acquired using the Bruker Esprit software with a probe current on the order of 1.5 nA and about 0.5 nm probe size.

For the local lattice mapping, the respective quantum dot image (the HRTEM image in Fig. 2c in the experimental case; and the atomistic figure in Extended Data Fig. 3a produced by taking a single atomic slice from a valence force field relaxed model in the theoretical case) was analysed using the image-processing algorithms developed in MATLAB. The original image was first filtered by means of a custom-made fast Fourier transform spatial filter, to reduce noise and identify the main lattice points. A particle detection algorithm available as part of the MATLAB image processing toolbox was then used to identify the peaks, from which the weighted centre of mass was extracted for each peak. The distances between peaks throughout the image were computed and were consequently normalized to the lattice of the CdS shell in order to determine the local lattice in normalized units.

To fabricate the lasing device, first the second-order distributed feedback hexagonal array was fabricated by spin-coating a thin layer of poly(methyl methacrylate) (PMMA; 950K A5) at 3,500 r.p.m. for 60 s onto the substrate and cured at 180 °C for 60 s. The PMMA was then coated with a thin layer (about 8 nm) of thermally evaporated aluminium for laser height alignment and charge dissipation. The PMMA was patterned using a Vistec EBPG 5000+ E-beam lithography system

into a two-dimensional hexagonal array of circles with a diameter of 160 nm and periodicity of 430 nm spacing between adjacent circular pillars. The aluminium layer was stripped using Developer 312. PMMA was developed using a 1:3 mixture of methyl isobutyl ketone (MIBK): isopropanol for 60 s. A 60 nm layer of MgF_2 was then thermally evaporated onto the device. For lift-off, the substrate was soaked in acetone overnight and then left in acetone for four hours followed by 30 min stirring and acetone rinse.

The devices were cleaned by oxygen plasma for 5 min. Chloride exchanged biaxially strained CQDs were spin-coated onto the PC-DFB array at a spin speed of 1,000 r.p.m. for 60 s and was exposed to air for one day. A protective layer of spin-on glass (which has characteristics similar to those of SiO_2) (Filmtronics 500F) was spin coated at 3,000 r.p.m. for 12 s and annealed in a N_2 atmosphere for 60 min at 100 °C.

The morphologies of the samples were investigated using SEM on a Hitachi SU-8230 apparatus with an acceleration voltage of 1 kV. The atomic force microscope measurements were performed using Asylum Research Cypher S operating in alternating-current contact mode.

The laser devices were adhered with thermal paste to a Peltier stage in order to assist further with thermal dissipation. The front surface of the Peltier was cooled to −26 °C, and a stream of compressed air was used to prevent frost building up. The resulting temperature of the device, in the absence of photoexcitation, was measured to be −20 (±0.2) °C using thermocouples. Optical pumping was achieved using one 442 nm 3 W laser diode. For pulsed operation, the continuous-wave photoexcitation was modulated using an acousto-optic modulator (IntraAction Corp., rise time about 300 ns). For continuous-wave photoexcitation, the acousto-optic modulator was used to constantly modulate the original beam, creating a second continuous wave at a different wave vector. The photoexcitation beam was focused onto the sample to a spot size of 30 μm × 50 μm. The emission was collected through two lenses into a single-mode fibre or a 50-μm fibre. The spectrum was measured using an Ocean Optics USB2000+ spectrometer. Transient emission measurements were taken by collecting the laser emission through two lenses into a 200-μm-diameter fibre, passing it through a monochromator (Photon Technology International, 600 lines mm^{-1}, 1.25 μm blaze, 1 mm slit widths) to filter out photoluminescence, and coupling it to a Si photodetector (Thorlabs DET 36A, rise time 14 ns). The photodetector response was measured using a 1 GHz oscilloscope. High-frequency noise was removed from the signal by a fast Fourier transform.

To enable study of ASE thresholds, we spin-coated CQD films at a spin speed of 3,000–1,000 r.p.m. for 60 s onto glass substrates. Films were exposed to air for one day before ASE characterization.

For nanosecond measurements, ASE was measured using a 1 ns pulse duration laser with a wavelength of 355 nm and frequency of 100 Hz. A cylindrical lens with 20 cm focal length was used to focus the beam to a stripe with dimensions of 2,000 μm × 10 μm. The sample was excited perpendicular to the surface of the film and the emission was collected parallel to the film surface from the edge of the sample. The emission was collected directly into a 50-μm-diameter multi-mode fibre. The emission spectrum was measured using an Ocean Optics USB2000+ spectrometer. The modal gain was measured using the variable stripe length method. The stripe width was 10 μm and the length was varied between 100 μm and 400 μm. The emission was collected directly into a 50 μm fibre, and the modal gain was determined using the ASE emission intensity versus stripe length relation using the equation $I(L) = A[e^{gL} - 1]/g$, where I is the ASE emission intensity, A is a constant proportional to spontaneous emission intensity, g is the modal gain and L is the stripe length.

For femtosecond measurements, ASE was measured using an approximately 250 fs pulse duration with a wavelength of 355 nm and a frequency of 5 kHz. These pulses were produced using a regeneratively amplified Yb:KGW laser (Light Conversion, Pharos) and an optical parametric amplifier (Light Conversion, Orpheus). A lens was used to defocus the beam into a circular spot of diameter about 1 mm, and emission was collected directly with a 50 μm fibre into an Ocean Optics USB2000+ spectrometer.

Simulation methods. Exciton fine-structure calculations were performed using the previously developed methodology[5,34] as implemented in QNANO. Single-particle electronic states of the quantum dots (CQDs) are computed within the tight-binding method, parametrized to reproduce the band structure of bulk CdSe and CdS calculated within the density functional theory methodology using VASP[35,36] including spin-orbit interactions and using PBE[37] exchange-correlation functional. The bandgap is then corrected to experimental value by shifting the conduction bands.

Parameters from fitting for wurtzite CdSe and CdS are presented in Supplementary Table 1. The sign convention for cation-anion and anion-cation hopping parameters follows that of ref. 38.

Strain dependence is included by adding the bond-stretching and bending dependence into tight-binding parameters[39], and fitting to density functional theory-derived valence and conduction band deformation potentials[40] (Supplementary Fig. 2). The strain-dependence parameters are summarized in Supplementary Table 1.

Nanocrystals are cut out from bulk wurtzite CdSe and CdS, using a 4 nm core and 10 nm total diameter. For the disk-shaped nanocrystals, the core is shifted off-centre by 2 nm and then 1 nm of CdS shell is shaved off on each side along the c-axis. Then the structure is relaxed (Extended Data Fig. 3a) using the valence force field method, using the elastic constants from Supplementary Table 1.

Similar to previous work for core-only nanocrystals[5], single-particle band-edge hole states consist of a 4-holes nearly degenerate manifold (plus spin degeneracy for each level), separated from the rest of the states by a small gap (Extended Data Fig. 3b). This manifold is split by 20 meV in the hydrostatically strained CQD and by 55 meV in a biaxially strained CQD.

Of these four hole levels, two have an *s*-orbital-like envelope and two are *p*-orbital-like (Extended Data Fig. 3b), resulting in two nominally bright and two dark transitions to the lowest-lying 1S electron state, respectively, as confirmed by the computed dipole transition elements. Electron states remain mostly localized in the core, for both types of strain. No polarization of the electron–hole pairs due to the piezoelectric field is noticeable (Extended Data Fig. 3b).

The exciton fine structure (Extended Data Fig. 3c, d) is computed using the configuration interaction method, using the basis of 8 (×2 for spin-degeneracy) electrons and 8 (×2) holes. The intensity of optical transitions between the obtained states is calculated based on the computed dipole transition elements. Computed biexciton binding energies are about 20 meV for both types of strain.

Ligand-binding energies are computed within density functional theory, using the CP2K computational package[41]. Goedecker–Tetter–Hutter pseudopotentials[42] with MOLOPT basis sets (possessing low basis set superposition errors)[43] and a 300 Ry grid cut-off were used. The ligands were placed on the Cd-terminated and Se-rich (0001) facets saturated with Cd adatoms of a Cd-rich 1.5 nm CdSe nanocrystal in a (30 Å × 30 Å × 30 Å) unit cell. The rest of the dangling bonds are fully saturated with carboxylate and amine ligands[44] to ensure the charge neutrality condition[45,46]. Desorption energies are reported relative to fully relaxed with no constraint structures and unprotonated anionic ligands (within a spin-polarized calculation). Octadecene is a non-polar solvent and thus no solvent dielectric constant was included in the calculations. Binding energies at 300 °C were corrected by computing the vibrational frequencies of the free and adsorbed ligands, and including the ensuing zero point energies, capacity and entropic contributions, following the standard thermochemistry protocols[47]. Ligands on the surface were computed in the harmonic limit while desorbed ligands were computed using the ideal gas approximation. The gas-phase entropy provides an overestimate of the translational and rotational degrees of freedom of ligands in a dense solvent (octadecene) and thus we rescale this contribution down to 30% of its gas-phase value.

For the analytical gain threshold model, we introduce an effective degeneracy factor of the band-edge hole states: $g_h = 2\sum\exp(-\Delta E/kT)$, where the factor 2 accounts for spin degeneracy, ΔE is the distance of the level from the band edge, and the sum is performed over 4 hole levels. In the limit of zero splitting it gives 8, whereas it is 2 in the case of large splitting.

The definition of the gain threshold in terms of quasi-Fermi level splitting overcoming the bandgap can be approximately recast in terms of the band-edge state occupancy, n_e and n_h, as follows: $n_e + n_h = 1$ or $N/g_e + N/g_h = 1$, where g_e and g_h are the effective degeneracies for electrons and holes, respectively, and N is the number of electron–hole pairs per dot.

In the case of twofold spin degenerate band-edge states, $g_{e,h} = 2$, so gain is achieved at $N = 1$. For eightfold-degenerate hole states, the gain threshold is $N = g_e g_h/(g_e + g_h) = 2 \times 8/(2 + 8) = 1.6$. In ensemble, $N = 1.6$ would mean that all dots should be populated with an exciton, and 0.6 of the dot population should contain one more exciton, that is, 0.6 of the dot population contains biexcitons and the remaining 0.4 contains excitons. However, in reality, it is impossible to populate the ensemble homogeneously, and some dots will contain more than two excitons while some will have no excitons at all, as described by the Poisson distribution (Extended Data Fig. 1a).

One can roughly estimate the effect of Poissonian statistics on the gain threshold by looking at what average occupancy $\langle N \rangle$ a ratio of emitting dots (biexcitons and multiexcitons) to absorbing dots (empty dots and dots with a single exciton) similar to that in the homogeneous distribution is achieved. For $N = 1.6$ the corresponding $\langle N \rangle \approx 2.3$.

To estimate the gain threshold more accurately, numerical gain threshold simulations were performed following the existing methodology[48] and extending it to include the eightfold degeneracy, inhomogeneous broadening of the levels, oscillator strengths of the transitions, and biexciton binding energy (Extended Data Fig. 1d, e). Splitting and oscillator strengths of the levels are chosen according to our tight-binding results and experimental ensemble line broadening is measured. The resulting excitons are populated according to Boltzmann statistics. Spin selection rules are used to modify the initial oscillator strengths, converting half

of the transitions into dark ones. Biexciton (un)binding energies ranging from 0 meV to 30 meV (as suggested by the theoretical model and experimental gain peak position) were included in the calculation.

For a given average occupancy $\langle N \rangle$ an analytical Poissonian distribution is taken into account. For continuous-wave excitation, the Poisson distribution accounting for carrier losses due to Auger recombination and photoluminescence is obtained from Monte Carlo simulations[28,49] (Extended Data Fig. 1a). Multiexcitons are assumed to have the same emission spectrum as biexcitons but no absorption, since the 1S electron state is fully bleached.

Our model agrees with the published results[48], predicting $\langle N \rangle = 1.15$ threshold for single-electron and hole levels (twofold spin-degenerate each). For eightfold-degenerate holes, we obtain $\langle N \rangle = 2.33$–2.55 with 20 meV splitting, 95 meV linewidth, while splitting the levels by 55 meV and narrowing the linewidth to 55 meV reduces the threshold to $\langle N \rangle = 1.77$–2.08 (Extended Data Fig. 1d, e). For the chosen set of parameters, oscillator strengths have the largest effect on the threshold, whereas inhomogeneous linewidth and biexciton binding energy do not affect the results practically.

In the continuous-wave regime, the gain thresholds appear to be lower than in the femtosecond regime owing to changes in the Poisson distribution (Extended Data Fig. 1b), which reduce the amount of empty dots and thus reduce the reabsorption. Increased temperature somewhat counterbalances this effect, producing final thresholds of about 2.1 and 1.6 average occupancies for the hydrostatic and biaxial strains, respectively. The value $\langle N \rangle$, however, is less informative in the continuous-wave regime as it provides no information on what external power would be required to reach this occupancy. We thus computed the external power required to achieve a given $\langle N \rangle$, as well as the amount of heat losses due to Auger recombination (Extended Data Fig. 1f), using a Monte Carlo model.

Data availability. Source Data are provided for Figs 3 and 4 and Extended Data Figs 1–9. All other data that support the findings of this study are available from the corresponding author upon request.

29. Carbone, L. *et al.* Synthesis and micrometer-scale assembly of colloidal CdSe/CdS nanorods prepared by a seeded growth approach. *Nano Lett.* **7,** 2942–2950 (2007).
30. Yu, W. W., Qu, L. H., Guo, W. Z. & Peng, X. G. Experimental determination of the extinction coefficient of CdTe, CdSe, and CdS nanocrystals. *Chem. Mater.* **15,** 2854–2860 (2003).
31. Coropceanu, I. & Bawendi, M. G. Core/shell quantum dot based luminescent solar concentrators with reduced reabsorption and enhanced efficiency. *Nano Lett.* **14,** 4097–4101 (2014).
32. Orfield, N. J., McBride, J. R., Keene, J. D., Davis, L. M. & Rosenthal, S. J. Correlation of atomic structure and photoluminescence of the same quantum dot: pinpointing surface and internal defects that inhibit photoluminescence. *ACS Nano* **9,** 831–839 (2015).
33. She, C. X. *et al.* Low-threshold stimulated emission using colloidal quantum wells. *Nano Lett.* **14,** 2772–2777 (2014).
34. Korkusinski, M., Zielinski, M. & Hawrylak, P. Multiexciton complexes in InAs self-assembled quantum dots. *J. Appl. Phys.* **105,** 122406 (2009).
35. Kresse, G. & Hafner, J. *Ab initio* molecular dynamics for liquid metals. *Phys. Rev. B* **47,** 558–561 (1993).
36. Kresse, G. & Joubert, D. From ultrasoft pseudopotentials to the projector augmented-wave method. *Phys. Rev. B* **59,** 1758–1775 (1999).
37. Perdew, J. P., Burke, K. & Ernzerhof, M. Generalized gradient approximation made simple. *Phys. Rev. Lett.* **77,** 3865–3868 (1996).
38. Jancu, J.-M., Scholz, R., Beltram, F. & Bassani, F. Empirical SPDS* tight-binding calculation for cubic semiconductors: general method and material parameters. *Phys. Rev. B* **57,** 6493–6507 (1998).
39. Boykin, T. B., Klimeck, G., Bowen, R. C. & Oyafuso, F. Diagonal parameter shifts due to nearest-neighbor displacements in empirical tight-binding theory. *Phys. Rev. B* **66,** 125207 (2002).
40. Li, Y. H., Gong, X. G. & Wei, S. H. Ab initio all-electron calculation of absolute volume deformation potentials of IV-IV, III-V, and II-VI semiconductors: the chemical trends. *Phys. Rev. B* **73,** 245206 (2006).
41. VandeVondele, J. *et al.* QUICKSTEP: fast and accurate density functional calculations using a mixed Gaussian and plane waves approach. *Comput. Phys. Commun.* **167,** 103–128 (2005).
42. Hartwigsen, C., Goedecker, S. & Hutter, J. Relativistic separable dual-space gaussian pseudopotentials from H to Rn. *Phys. Rev. B* **58,** 3641–3662 (1998).
43. VandeVondele, J. & Hutter, J. Gaussian basis sets for accurate calculations on molecular systems in gas and condensed phases. *J. Chem. Phys.* **127,** 114105 (2007).
44. Beecher, A. N. *et al.* Atomic structures and gram scale synthesis of three tetrahedral quantum dots. *J. Am. Chem. Soc.* **136,** 10645–10653 (2014).
45. Voznyy, O. *et al.* A charge-orbital balance picture of doping in colloidal quantum dot solids. *ACS Nano* **6,** 8448–8455 (2012).
46. Voznyy, O. Mobile surface traps in CdSe nanocrystals with carboxylic acid ligands. *J. Phys. Chem. C* **115,** 15927–15932 (2011).
47. Cramer, C. J. *Essentials of Computational Chemistry: Theories and Models* Ch. 10 (John Wiley & Sons, 2013).
48. Park, Y. S., Bae, W. K., Baker, T., Lim, J. & Klimov, V. I. Effect of auger recombination on lasing in heterostructured quantum dots with engineered core/shell interfaces. *Nano Lett.* **15,** 7319–7328 (2015).
49. Korkusinski, M., Voznyy, O. & Hawrylak, P. Theory of highly excited semiconductor nanostructures including auger coupling: exciton-biexciton mixing in CdSe nanocrystals. *Phys. Rev. B* **84,** 155327 (2011).

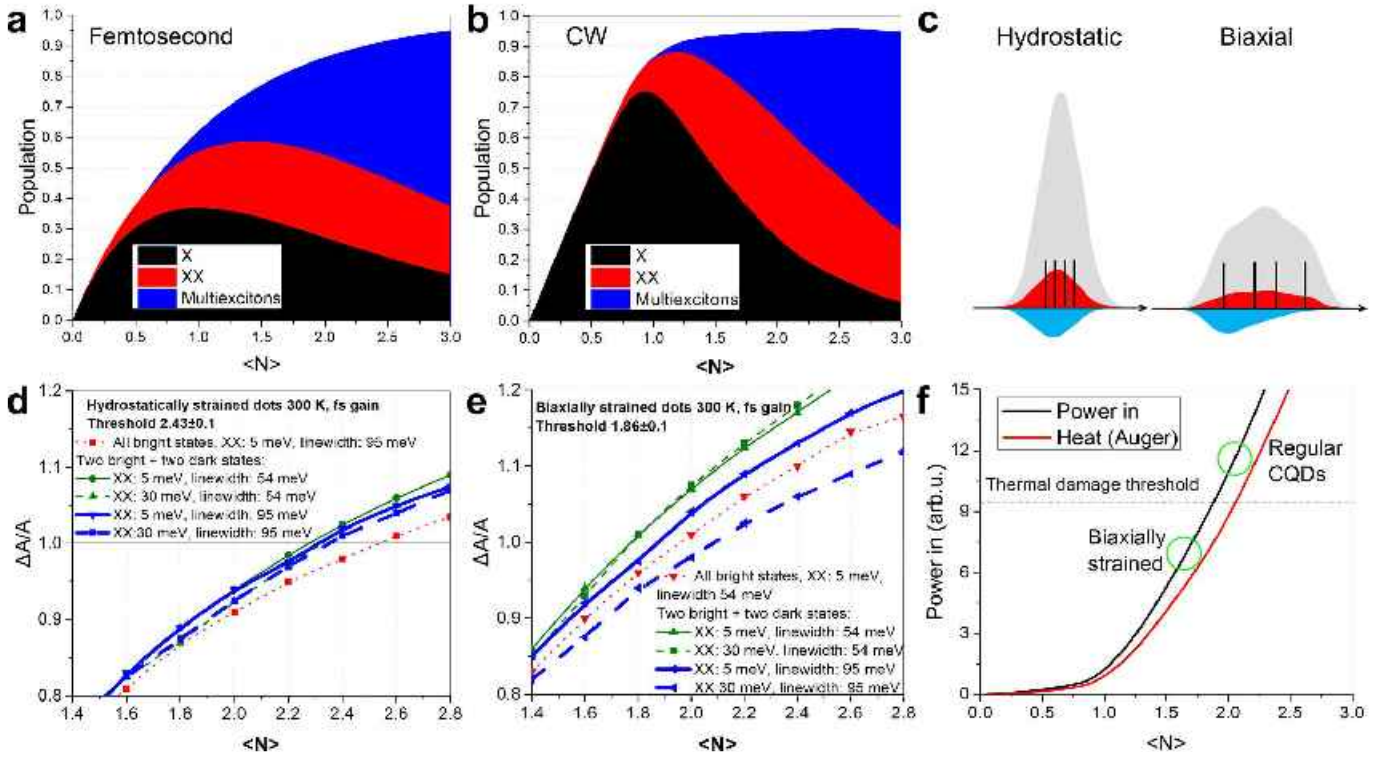

Extended Data Figure 1 | Numerical simulations. a, **b**, Poisson distribution of single-exciton (X), biexciton (XX) and multiple excitons in CQD ensembles with different average exciton occupations $\langle N \rangle$ under femtosecond (**a**) and continuous-wave (**b**) photoexcitations. **c**, Competition between stimulated emission (blue) and absorption (red) at $\langle N \rangle = 2.0$ exciton population for ensembles. Hydrostatically strained (below the threshold) and biaxially strained (above the threshold) quantum dots. Grey indicates absorption at zero state filling, red indicates absorption of populated dots ensemble, and blue indicates stimulated emission. Black lines indicate excitonic energies and oscillator strengths. **d**, **e**, Numerical simulation of absorption bleaching and gain versus exciton occupancy in hydrostatically (**d**) and biaxially (**e**) strained CQDs for different hole degeneracies, splitting values and linewidths. **f**, Numerical simulation showing the dependence of excitation power required to maintain the given occupancy in the continuous-wave regime. A 1.4× gain threshold reduction in terms of excitonic occupancy reduces the required power about 1.7× in the continuous-wave regime. Reducing the gain threshold is critical for realizing continuous-wave lasing. More than 80% of the incident power aimed at achieving population inversion is converted to heat owing to Auger recombination losses.

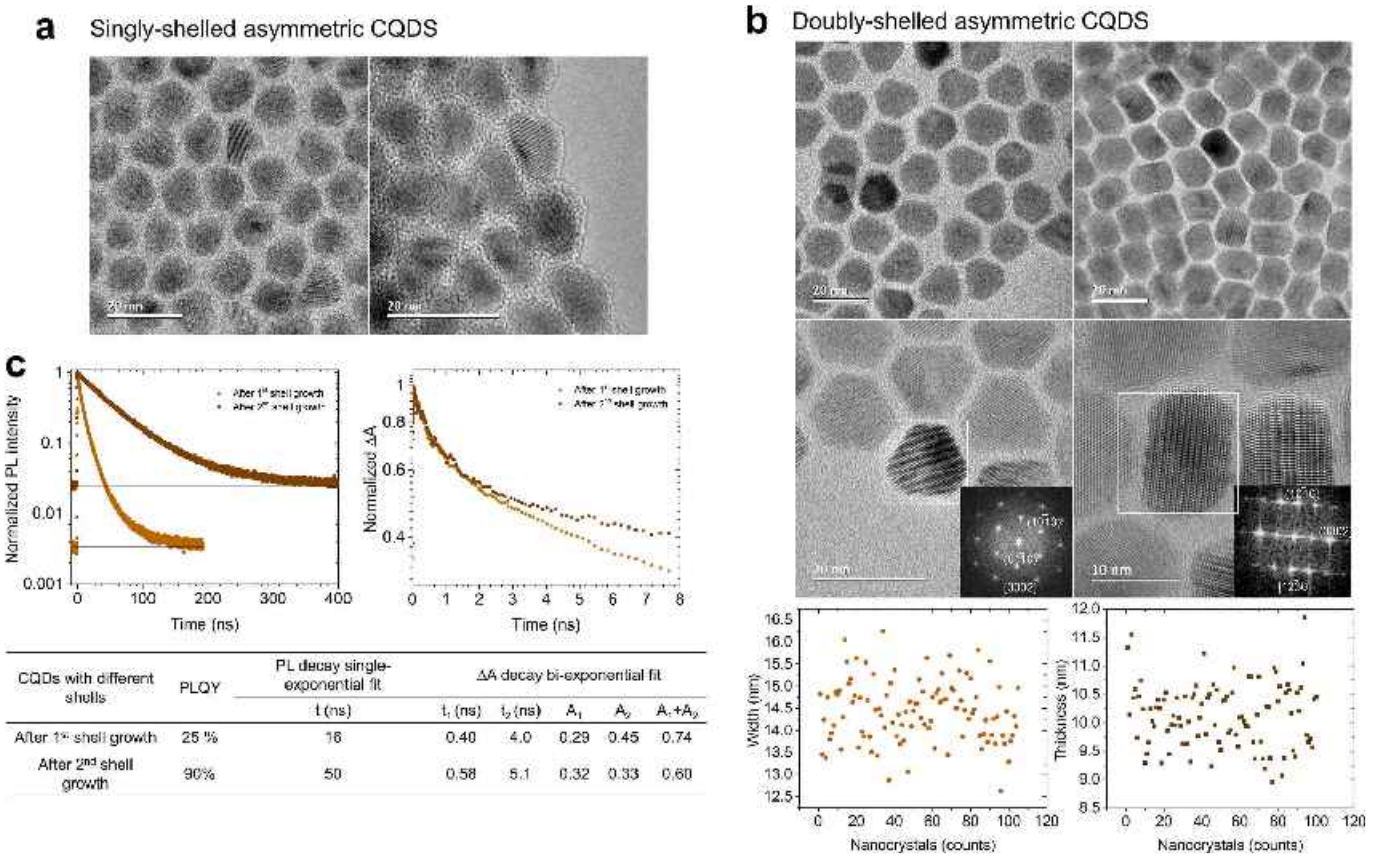

CQDs with different shells	PLQY	PL decay single-exponential fit	ΔA decay bi-exponential fit				
		τ (ns)	τ_1 (ns)	τ_2 (ns)	A_1	A_2	A_1+A_2
After 1st shell growth	25 %	16	0.40	4.0	0.29	0.45	0.74
After 2nd shell growth	90%	50	0.58	5.1	0.32	0.33	0.65

Extended Data Figure 2 | TEM images and exciton decay dynamics of singly and doubly shelled biaxially strained CQDs. a, Bright-field TEM and HRTEM characterizations of singly shelled asymmetric CQDs. TEM images unveil the hemispherical shape of asymmetric CQDs, which directly confirms that only (0001) facet growth has been blocked by oleylamine when TOPS was used as a sulfur precursor. **b**, Bright-field TEM and HRTEM characterizations of doubly shelled asymmetric CQDs. To get an overall morphology characterization, doubly shelled CQDs were deposited on lacey-carbon TEM grids with holes to observe CQDs with different orientations. A thorough analysis reveals that these CQDs (nanocrystals) show hexagonal disk-like shapes with two flat faces: viewing from the [0002] zone axis, they show hexagonal or triangular shapes; observing along the [12$\bar{3}$0] axis, they show rectangular shapes with two curved sides. The fast Fourier transform patterns (insets) were obtained from the boxed areas. **c**, Single- and multiple-exciton lifetimes of asymmetric CQDs with single and double shells, respectively. After the second uniform shell growth, fast non-radiative trap recombination is dramatically eliminated, resulting in greatly lengthened single-exciton lifetime (left) and increased PLQY. The multi-exciton dynamics (right) were investigated by ultrafast transient absorption spectroscopy. To achieve the same exciton population, only the CdSe cores were photoexcited (2.18 eV, 570 nm, 507 μJ cm^{-2}). Owing to improved passivation, the amplitude of the slower decay (t_2), which can be attributed to trion Auger recombination, decreases notably in doubly shelled asymmetric CQDs, indicating that photoionization has been partially suppressed. As a result, more excitons were retained in doubly shelled CQDs over the entire time regime investigated (0–8 ns). (In all figures, normalizations were performed as follows: maximum scaled to 1, minimum not rescaled.)

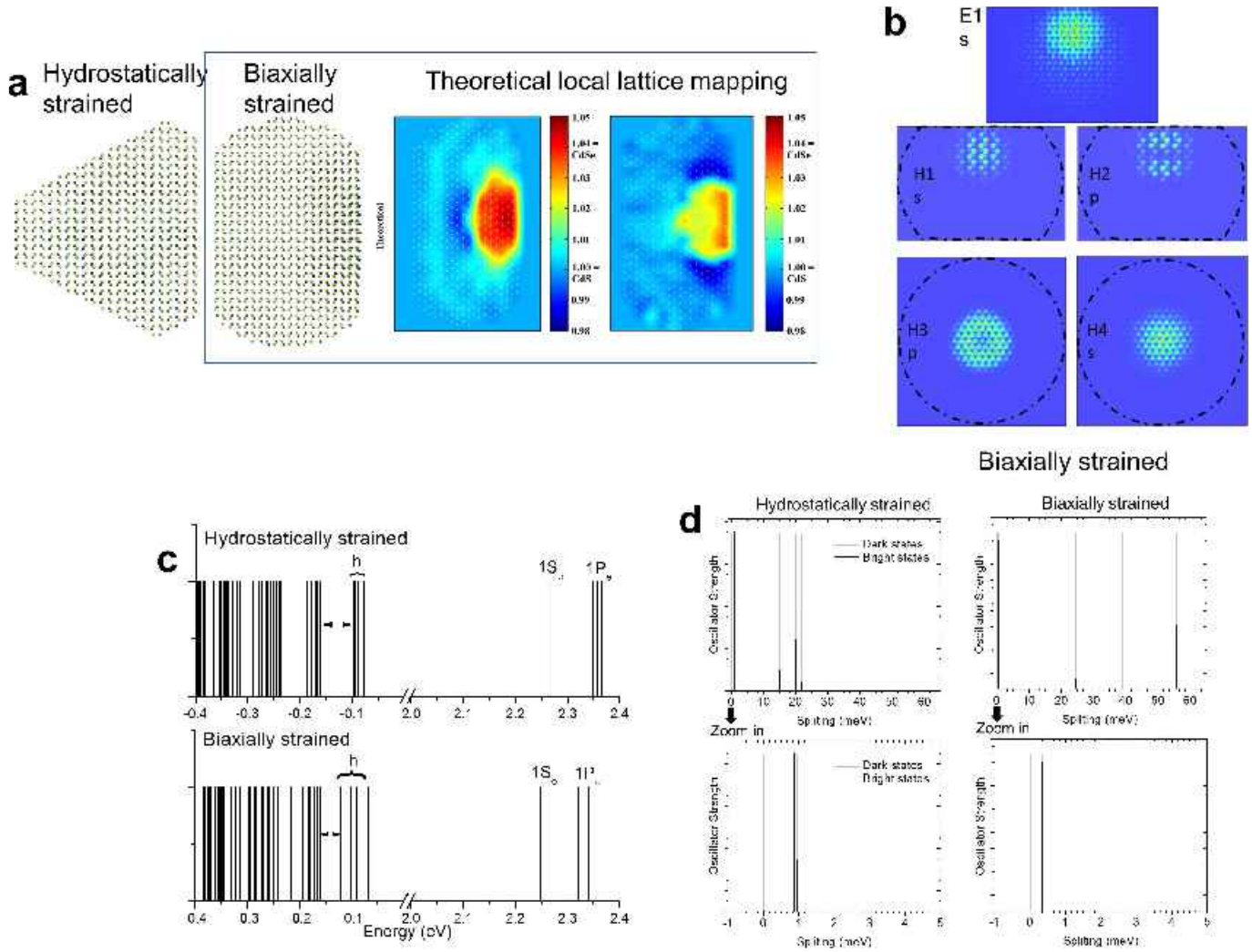

Extended Data Figure 3 | Band and exciton fine structures simulations. **a**, Core-shell structures following the strain relaxation procedure. The left panel shows a tetrahedron shape, with the 4 nm CdSe core exactly at the centre, leading to hydrostatic strain. the right panel shows a disk shape, with the 4 nm CdSe off-centre by 2 nm, leading to biaxial strain. The local lattice constant mapping of the simulated biaxially strained core–shell structure is plotted here for comparison with experimental results in Fig. 2c. **b**, Wavefunctions of the topmost electron (E1) and hole states (H1, H2, H3, H4) in the biaxially strained CQDs. **c**, Single-particle states of hydrostatically and biaxially strained CdSe-CdSe core–shell quantum dots calculated with the tight-binding method (h is the manifold of four hole states). **d**, Exciton fine structures from tight-binding atomistic simulations. The lowest dark state originates from the spin-forbidden configuration based on the heavy hole. The lowest dark–bright splitting depends on the electron–hole exchange interaction, which remains on the order of 1 meV in thick-shell dots and is not affected by the splitting between the heavy-hole and light-hole states; that is, it is insensitive to biaxial strain.

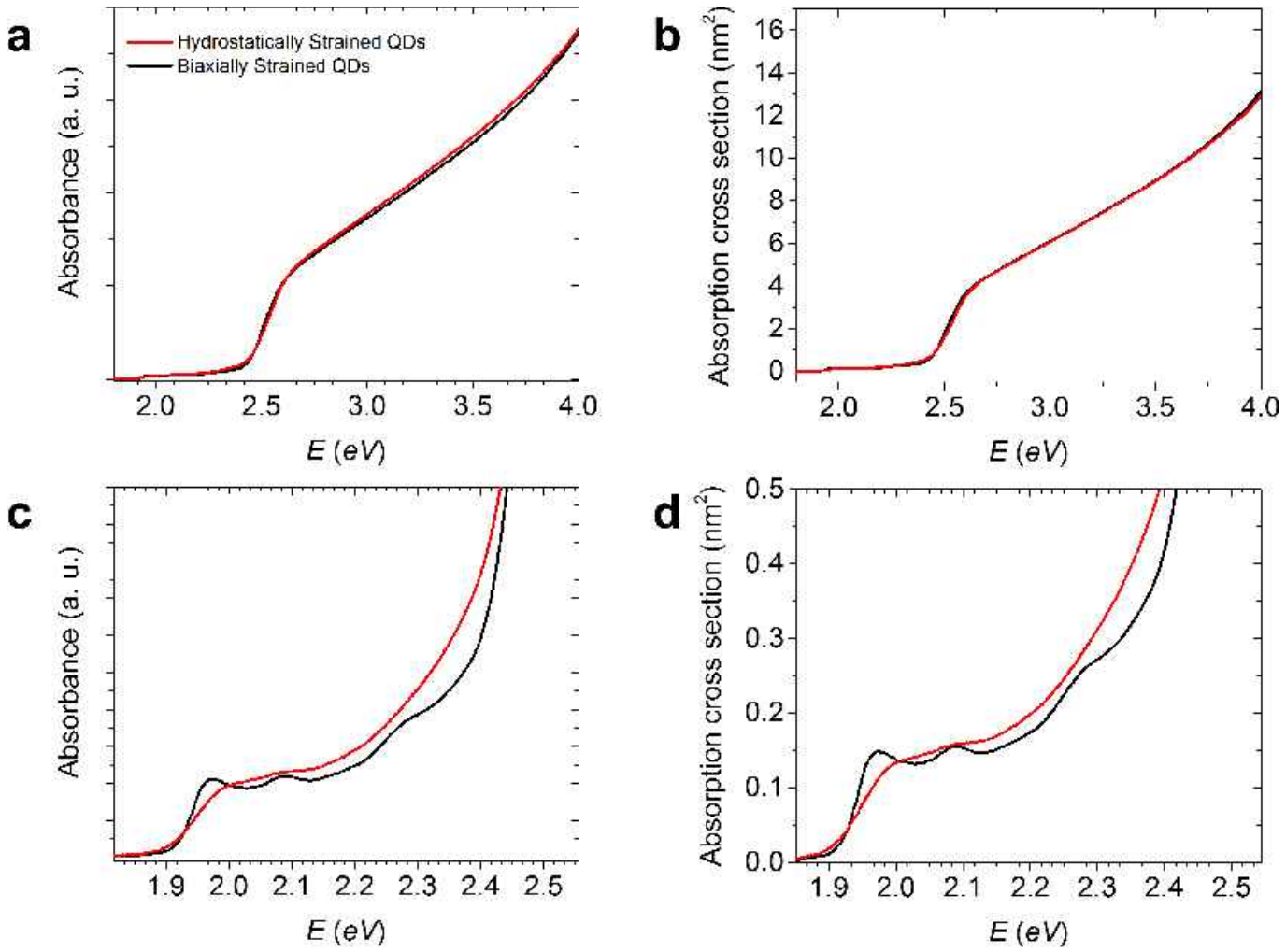

Extended Data Figure 4 | Full absorbance spectra and absorption cross-sections of hydrostatically and biaxially strained CQDs. a, **b**, Full-scale spectra. **c**, **d**, Spectra with exciton peaks zoomed in. See Methods for absorption cross-section measurement details.

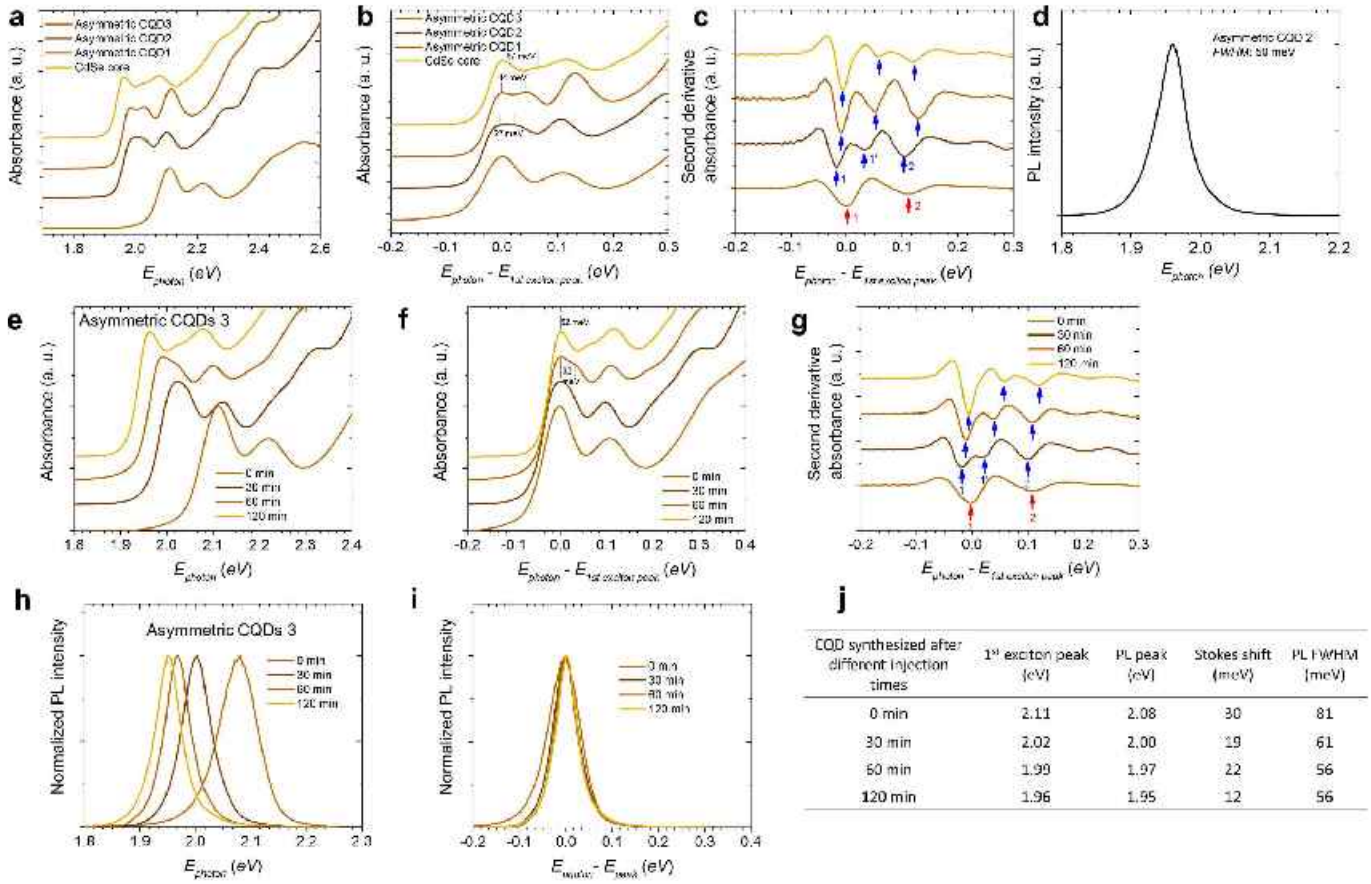

j

CQD synthesized after different injection times	1st exciton peak (eV)	PL peak (eV)	Stokes shift (meV)	PL FWHM (meV)
0 min	2.11	2.08	30	81
30 min	2.02	2.00	19	61
60 min	1.99	1.97	22	56
120 min	1.96	1.95	12	56

Extended Data Figure 5 | Absorbance spectra, their second derivatives and photoluminescence spectra of CQDs with varying degrees of splitting. **a**–**c**, Samples named asymmetric CQD1, CQD2 and CQD3; see synthetic details in the Methods. Asymmetric CQD3 is the single-shell CQD mentioned in the main text. Blue and red arrows highlight the peak positions. **d**, Photoluminescence spectrum of asymmetric CQD2. **e**–**i**, Absorbance and photoluminescence spectra evolution during first-shell growth; the resulting product is asymmetric CQD3. **e**, **f**, During the growth of the first asymmetric shell, the first exciton peak gradually broadens and then splits into two peaks with increasing reaction time, reaching a maximum splitting of 62 meV. At the same time, the band-edge exciton peak continuously redshifts as a result of increased electron wave function delocalization. **g**, The progressive splitting is more obvious in the second-derivative absorbance spectra. **h**, **i**, The photoluminescence linewidths dramatically decrease after shell growth and photoluminescence peaks redshift as the band-edge exciton peaks shift. **j**, A summary of data from **e**–**f**.

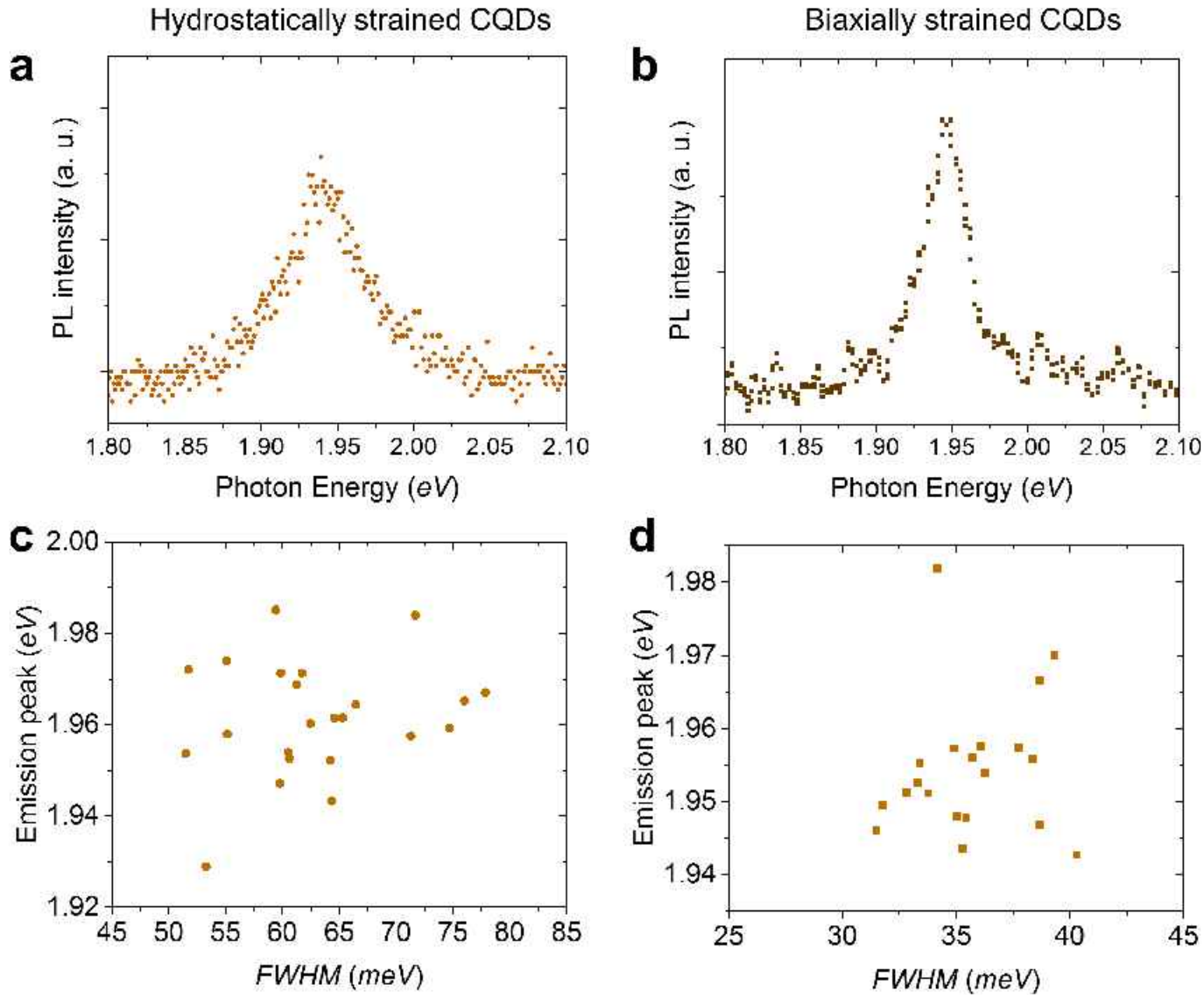

Extended Data Figure 6 | Single-dot photoluminescence linewidth measurement. a, **b**, Typical single-dot spectra of hydrostatically (**a**) and biaxially (**b**) strained CQDs, with FWHMs of 60 meV and 32 meV, respectively. **c**, 24 hydrostatically strained CQDs show average photoluminescence linewidth of 63 meV and peak position of 1.96 eV, with standard deviations of 11.8% and 0.67%, respectively. **d**, The average photoluminescence linewidth and peak position of 20 biaxially strained single dots are 36 meV and 1.95 eV, with standard deviations of 7.2% and 0.5%, respectively. The binning time of the single-dot photoluminescence linewidth measurement is 50 ms.

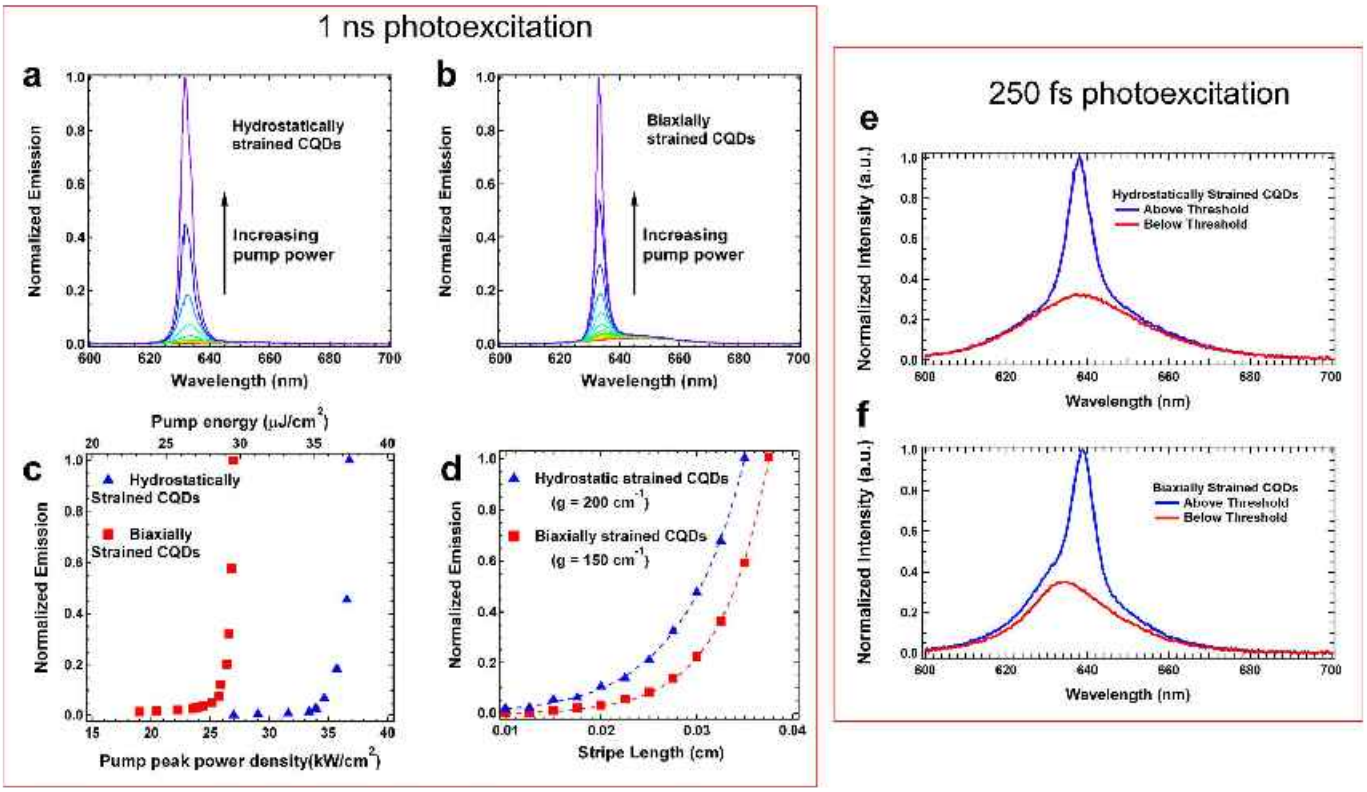

Extended Data Figure 7 | ASE threshold, and modal gain measurements of CQDs films. a, **b**, Spectra of hydrostatically (**a**) and biaxially (**b**) strained CQDs, respectively, with increasing photoexciting power, showing ASE peaks rising above the photoluminescence background. **c**, Emission as a function of photoexciting peak power density and pulse energy for both hydrostatically and biaxially strained CQDs. A 2 mm × 10 μm stripe with 3.49 eV (355 nm) photoexcitation energy and 1 ns pulse duration was used. The ASE thresholds are 36 μJ cm^{-2} and 26 μJ cm^{-2} for hydrostatically and biaxially strained CQDs, respectively. **d**, Variable stripe length measurements for both hydrostatically and biaxially strained CQDs. Measurements were carried out using a photoexciting energy of four times the threshold value, obtained using a 2 mm × 10 μm stripe. The gain values *g* are 200 cm^{-1} and 150 cm^{-1} for hydrostatically and biaxially strained CQDs, respectively. The lower gain value from biaxially strained CQDs can be explained by the fact that fewer emission states are participating in the optical gain. **e**, **f**, ASE threshold measurements of CQD films with 250 fs and 3.49 eV (355 nm) photoexcitation. Thresholds of 22 μJ cm^{-2} and 14 μJ cm^{-2} were determined from hydrostatically (**e**) and biaxially (**f**) strained CQD films used for measuring the 1 ns ASE threshold.

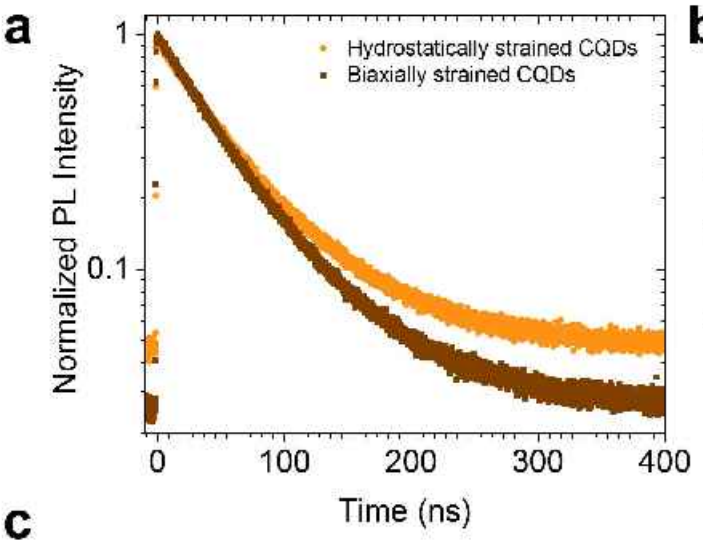

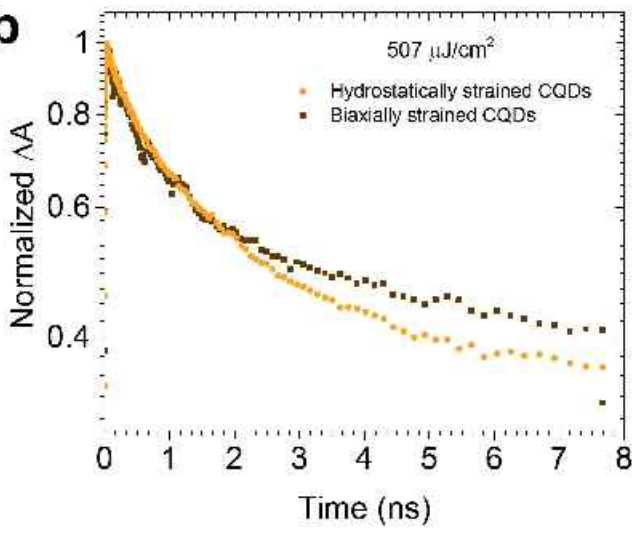

c

CQDs	PL QY	PL decay single-exponential fit	ΔA decay bi-exponential fit				
		t (ns)	t_1 (ns)	t_2 (ns)	A_1	A_2	A_1+A_2
Hydrostatically strained	80%	52	0.6 ns	3.3 ns	0.28	0.39	0.67
Biaxially strained	90%	50	0.58 ns	5.1 ns	0.32	0.33	0.60

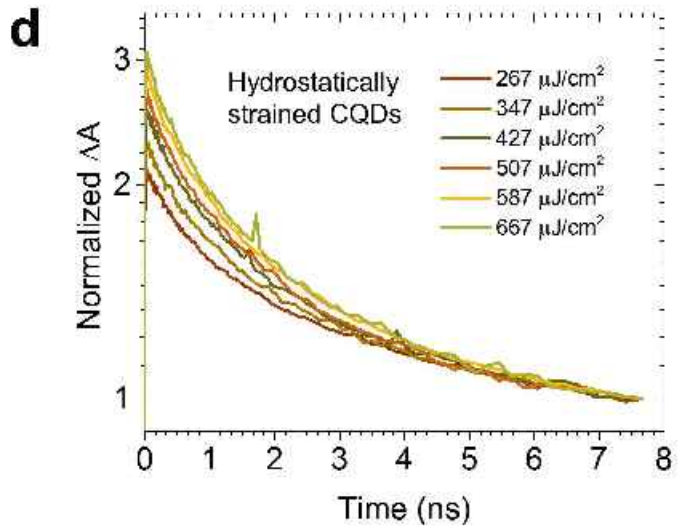

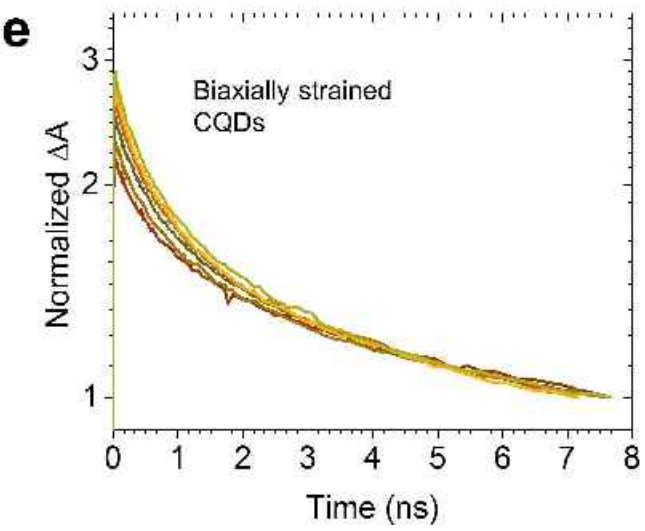

Extended Data Figure 8 | Single- and multiple-exciton lifetimes of hydrostatically and biaxially strained CQDs, respectively. a, Owing to the similar total shell volume, both types of core–shell CQDs show similar single-exciton lifetimes. **b**, The multiple exciton decays with core-only photoexcitation (2.18 eV, 570 nm, 507 μJ cm^{-2}) can be fitted as bi-exponential decays (**c**): in the fast decay regime, hydrostatically strained core–shell CQDs show slightly longer lifetime than the biaxially strained CQDs, but the opposite is true in the slower decay regime. Since multiple exciton decays are dominated by Auger recombination, the decay rates and amplitudes measured from transient absorption are much higher than those of the single-exciton radiative recombination measured using the TCSPC system. **d**, **e**, Multiple exciton decays under different photoexcitation intensities. The bleach signals time traces of hydrostatically strained and biaxially strained CQDs show clear dependence upon photoexcitation power, confirming that Auger recombination is the main decay path.

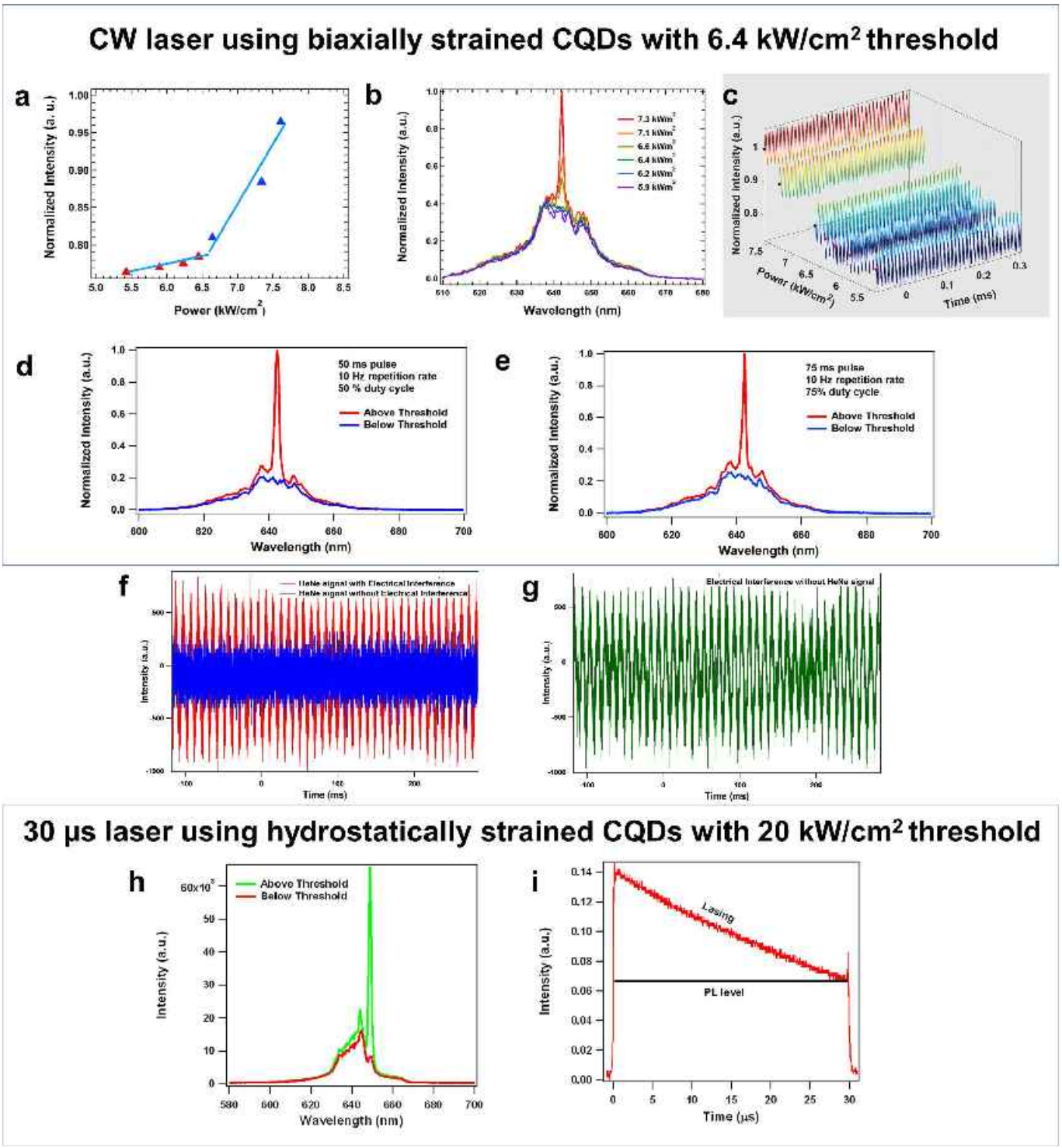

Extended Data Figure 9 | Continuous-wave PC-DFB CQD lasers with biaxially strained and hydrostatically strained CQDs. a, Normalized integration of the emitted signal (shown in Extended Data Fig. 9c) as a function of power under optical photoexcitation at 2.81 eV using a continuous-wave laser. **b**, Spectra at varying pump powers. **c**, Time traces of normalized emission intensity of the PC-DFB laser as a function of input excitation power with continuous-wave excitation. **d**, Emission spectra at powers above and below the threshold for 50 ms pulses and 10 Hz repetition rate, constituting a 50% duty cycle; **e**, Emission spectra at powers above and below the threshold for 75 ms pulses and 10 Hz repetition rate, constituting a 75% duty cycle. These data were collected by applying a delay to the spectrometer acquisition and measuring the spectra of the last ten microseconds of the pulse. **f**, HeNe laser (633 nm) signal with electrical interference induced by the acousto-optic modulator driver in the photodiode signal with alternating-current coupling (the measured HeNe laser signal is continuous wave with steady output). **g**, Electrical signal in the photodiode with no input radiation, showing electrical interference. The oscillation (102 Hz) in these traces and in lasing experiments is consistent, and caused by electrical interference, rather than changes in intensity. **h**, Emission spectra of PC-DFB lasers made from hydrostatically strained CQDs at powers above and below the threshold for 30 µs pulses and 10 Hz repetition rate, **i**, Transient behaviour of the lasing intensity for 30 µs at 20 kW cm^{-2}.

Extended Data Table 1 | Density-functional-theory ligand-binding energies on different CdSe facets

Binding energy (eV)	TOPS	Amine	Thiol
Cd(0001)	0	0.6±0.1	2.8±0.2
Se(000-1) + Cd adatoms	0.5±0.1	0.6±0.1	3±0.2
{10-10} facets	0.5±0.1	0.6±0.1	2.8±0.2
Cd(0001) at 300 °C	0	0.2±0.1	
Se(000-1) + Cd adatoms at 300 °C	0.2±0.1	0.2±0.1	